Simulations of Direct Ion Acceleration with Beating Electrostatic Waves

IEPC-2011-212

Bayard G. Gardineer, IV[*] , Benjamin Jorns[†] , and Edgar Y. Choueiri[‡]

Electric Propulsion and Plasma Dynamics Laboratory, Princeton University, Princeton, NJ, 08540, USA

A theoretical and numerical investigation of the Beating Wave Thruster (BWT) – an electrodeless electric propulsion concept based on direct ion acceleration with beating electrostatic waves (BEW) – is presented. Simulations reveal that in a collisionless ion ensemble, a rectilinear magnetic slope configuration generates a net linear ion current that flows along the magnetic null. Monte Carlo methods are used to demonstrate that BEW propagation can significantly enhance overall thruster performance by increasing both the magnitude and density of said current, while also revealing a unique phenomenon referred to as "ion channeling," in which stochastic ions are preferentially transported away from the thruster walls and towards the magnetic null. Single and beating wave cases are compared for equal wave energy densities and BEW superiority is demonstrated for the chosen wave parameters. Neglecting ambipolar effects, conservative thrust density and specific impulse estimates are calculated and shown to be comparable to many existing Hall and ion thruster configurations.

Nomenclature

$\mathbf{B}$	magnetic field	θ	Larmor phase angle
δ	half-width of magnetic slope	$\overline{\rho}$	normalized RMS Larmor radius
$\overline{\delta}$	normalized half-width of magnetic slope	Y_{GC}	guiding center Y-position
$\overline{r}_L$	root-mean-square (RMS) Larmor radius	L	thruster bound
ω_{ci}	ion cyclotron frequency	ξ_f	fraction of forward-drifting ions
h	Hamiltonian	ξ_{esc}	fraction of ions that escape to the walls
$\overline{\mathcal{H}}_k$	k-normalized action-angle Hamiltonian	ξ_{ex}	fraction of ions that breach the exit plane
$\mathcal{H}_{\overline{r}_L}$	$\overline{r}_L$-normalized Hamiltonian	U_{ex}	normalized exhaust velocity
$\mathbf{P}$	normalized momentum	n	ion density
$\overline{\mathbf{A}}$	normalized magnetic vector potential	T_r	ratio of electron to ion temperature (T_e/T_i)
E_0	electric field amplitude	I_{sp}	specific impulse
k	wave number	T/ℓ	thrust density
ω_i	frequency of ith wave	τ	normalized time
ε	normalized wave amplitude	ρ_{th}	stochastic Larmor radius threshold
κ	normalized wave number	ρ_f	forward-drifting Larmor radius threshold
ν_i	normalized frequency of ith wave	Z	ion charge (in units of e)
V_{eff}	effective potential	$|Y_{UB}|$	Y upper bound for forward-drifting ions
ρ	normalized Larmor radius	ν_c	ion collision frequency

---

[*]Undergraduate Researcher, MAE Dept., bgardine@mit.edu
[†]Graduate Researcher, MAE Dept., bjorns@princeton.edu
[‡]Chief Scientist, EPPDyL, Professor, Applied Physics Group, MAE Dept., choueiri@princeton.edu

I. Introduction

In 2010, Jorns and Choueiri proposed a new electric propulsion concept based on direct ion acceleration with beating electrostatic waves (BEW).[1] Inspired by a naturally-occurring phenomenon first observed in the upper ionosphere in the late 1970s,[2] the concept relies on BEW propagation to augment the linear ion current generated in a thermalized ion ensemble by a steeply-sloped rectilinear magnetic field. The ultimate goal is for this acceleration mechanism to form the basis of a new plasma propulsion system called the Beating Wave Thruster (BWT). The BWT has three principal characteristics that render it an attractive propulsion device:

1) ***Improved Lifetime*** – Electrode erosion hinders thruster performance and can lead to structural failure. As a consequence, it is a life-limiting process for many thruster classes, including MPD, ion, and Hall effect thrusters.[3,4] Since the BWT concept is electrodeless, it offers the potential benefit of improved lifetime over other electric thruster configurations.

2) ***High Efficiency*** – As an electric propulsion device, the BWT is expected to have a specific impulse that is superior to chemical rockets. Furthermore, as will be shown in Section III, BEW propagation triggers an "ion channeling" mechanism that tends to preferentially transport ions away from the thruster walls. This will serve to limit plasma-wall interactions, a source of appreciable energy losses in Hall and electrothermal thrusters.[5]

3) ***Variable Thrust and Specific Impulse*** – The BEW acceleration mechanism is affected by the frequency, amplitude, and wave number of the exciting waves.[6] Therefore, it is expected that variations in these parameters will correspond to changes in BWT specific impulse and thrust density. The ability to actively manipulate these parameters is advantageous from a mission optimization standpoint, both in terms of thruster versatility and overall power consumption.[7]

The goal of this paper is to demonstrate the potential of the BWT as a viable electric propulsion concept by building upon the foundational work of Jorns and Choueiri via simulation and numerical analysis. The paper is structured as follows: in Section II, we introduce the basic thruster concept in the absence of BEW (the "unperturbed" case), including the magnetic slope configuration, single-ion dynamics, and benchmark thruster characteristics. In Section III, we begin with a brief introduction of the BEW phenomenon and continue with an investigation of thruster performance in the presence of BEW (the corresponding "perturbed" case). We describe the effects of BEW propagation on ion trajectories and thruster characteristics, using Monte Carlo methods to determine preliminary BWT specific impulse, thrust density, and wall loss estimates. In Section IV, we summarize the major results of our investigation, and conclude with a brief discussion of recommended future work.

II. Basic Thruster Concept

A. Magnetic Field Topography

Critical to the success of the BWT concept is the topography of the applied magnetic field. A rectilinear, z-oriented field was chosen for this application, with a magnetic null at $y = 0$, a steep positive slope for $|y| < \delta$, and constant $\mathbf{B}$ for $|y| > \delta$. The hyperbolic tangent function exhibits these properties when scaled by the appropriate factors, yielding the following expression for the ideal applied magnetic field within the bounds of the thruster (see Figure 1):

$$\mathbf{B} = B_0 \tanh \frac{3y}{\delta} \hat{z} \tag{1}$$

This antisymmetric field configuration is intended to generate thrust by exploiting the gyromotion of ions in the vicinity of the magnetic null. Let us consider the behavior of a single ion in the unperturbed case. While the ion is in a homogenous field region ($y > |\delta|$), it traces out a simple Larmor trajectory. However, as it approaches the sloped region and begins to encounter B-field asymmetry, its trajectory becomes more complex. If the ion crosses the null ($y = 0$), the direction of the Lorentz force is reversed, resulting in mirrored orbits that propagate along $y = 0$ in the $\pm x$-direction. If the ion enters the sloped region but does not cross $y = 0$, it will experience a net ∇B drift in the $-x$-direction while remaining trapped on one side
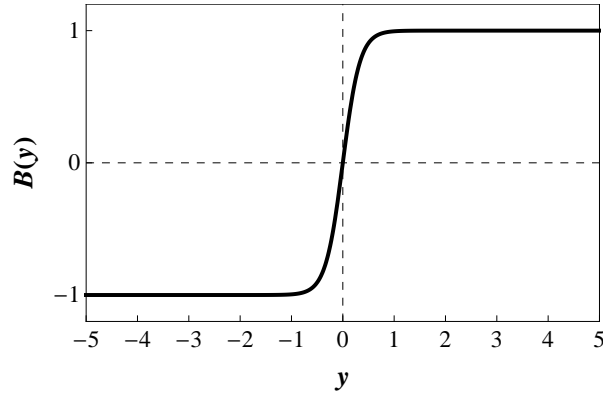
Figure 1. Magnetic field configuration as described by Eq. 1 for $B_0 = \delta = 1$. Note that the field is (approximately) homogeneous for $|y| > \delta$.

of the null. Jorns and Choueiri posited that for a thermalized ion distribution with an exit plane in the $\hat{x}$ direction, this sloped configuration would yield a net ion current in the $+x$-direction (and therefore, net thrust in the $-x$-direction) along the magnetic null, and proposed the introduction of BEW as a means of effectively augmenting that current.[1]

B. Unperturbed Ion Dynamics

Since unperturbed ion dynamics are just a special case of perturbed ion dynamics (with zero wave amplitude), we begin with the Hamiltonian of a magnetized ion of mass m and charge q subject to a spectrum of n perpendicularly propagating electrostatic waves:

$$h = \frac{1}{2m}(\mathbf{p} - q\mathbf{A})^2 + \frac{qE_0}{k}\sum_{i=1}^{n}\cos(kx - \omega_i t) \tag{2}$$

where $\mathbf{p}$ is the canonical momentum vector, $\mathbf{A}$ is the magnetic vector potential (such that $\nabla \times \mathbf{A} = \mathbf{B}$), E_0 is the wave amplitude, k is the wave number, and ω_i are the wave frequencies. For simplicity, we have assumed that all exciting waves are of equal amplitude, wave number, and phase.

Next, we nondimensionalize h via canonical transformation. First, however, for the purpose of normalization we introduce an exogenous quantity $\overline{r}_L$, the root-mean-square (RMS) Larmor radius of a hypothetical ion ensemble. After normalizing length to $\overline{r}_L$ and time to ω_{ci}^{-1}, we obtain the following expression for the $\overline{r}_L$-normalized Hamiltonian:

$$\mathcal{H}_{\overline{r}_L} = \frac{1}{2}\left([P_X - \overline{A}_X]^2 + P_Y^2\right) + \frac{\varepsilon}{\kappa}\sum_{i=1}^{n}\cos(\kappa X - \nu_i \tau) \tag{3}$$

where

$$\mathcal{H}_{\overline{r}_L} = \frac{1}{m\omega_{ci}^2\overline{r}_L^2}h \qquad \tau = \omega_{ci}t \qquad \nu_i = \frac{\omega_i}{\omega_{ci}} \qquad \kappa = k\overline{r}_L \qquad \varepsilon = \frac{qE_0}{m\omega_{ci}^2\overline{r}_L}$$

$$X = \frac{x}{\overline{r}_L} \qquad Y = \frac{y}{\overline{r}_L} \qquad \overline{A}_X = \frac{q}{m\omega_{ci}\overline{r}_L}A_x(\overline{r}_L Y) \qquad P_X = X' + \overline{A}_X \qquad P_Y = Y'$$

and the prime ($'$) denotes differentiation with respect to τ. This $\overline{r}_L$-normalization scheme will ultimately allow us to simulate ensemble behavior without having to specify a specific ion temperature.

The magnetic slope configuration described in Eq. (1) can also be expressed in $\overline{r}_L$-normalized coordinates:

$$\mathbf{B} = B_0\tanh\frac{3Y}{\overline{\delta}}\hat{z} \tag{4}$$

where $\overline{\delta} = \delta/\overline{r}_L$.

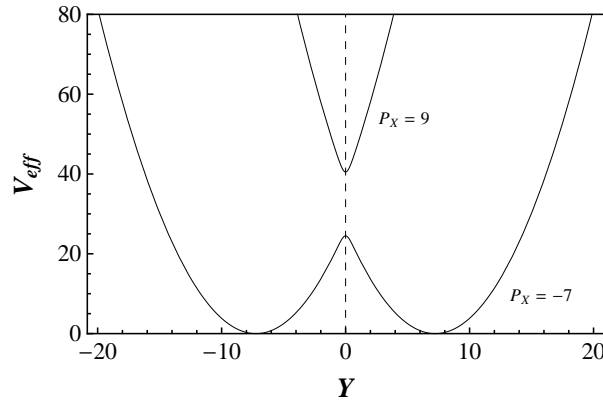In the unperturbed case, $\varepsilon = 0$ and the simplified Hamiltonian becomes

Figure 2. Plot of V_{eff} ($\bar{\delta} = 1$) for $P_X = 9$ and $P_X = -7$. **Note the single well behavior for $P_X > 0$ and the double well behavior for $P_X < 0$.**

$$\mathcal{H}_{\bar{r}_L} = \frac{1}{2}\left(\left[P_X - \overline{A}_X\right]^2 + P_Y^2\right) \tag{5}$$

Following the convention of Jorns and Choueiri,[1] since $\mathcal{H}_{\bar{r}_L}$ and P_X are constants of motion, we can express the Hamiltonian in terms of P_Y and an effective potential V_{eff} such that

$$V_{eff} = \frac{1}{2}\left(\left[P_X - \overline{A}_X\right]^2\right) \tag{6}$$

V_{eff} takes two forms depending upon the sign of P_X. For $P_X > 0$, the effective potential is a single well symmetric about $Y = 0$. For $P_X < 0$, V_{eff} becomes a symmetric double well with minima on the Y-axis and a local maximum at $Y = 0$ (see Figure 2).

The structure of this potential defines ion behavior in the unperturbed case. Jorns and Choueiri were able to classify particle trajectories based upon the sign of P_X and the value of the Hamiltonian $\mathcal{H}_{\bar{r}_L}$ for a given ion.[1] Their conclusions are summarized in the sections to follow. Subsequent analysis assumes $\bar{\delta} = 1$ unless otherwise noted.

1. $P_X > 0$

For an ion with $P_X > 0$, the effective potential is a symmetric single well with a minimum at $Y = 0$. All ions with $P_X > 0$ are trapped in this single well. The Y-bounds of their trajectories (and thus, the turning points) are given by $V_{eff} = \mathcal{H}_{\bar{r}_L}$. However, while for a uniform B-field this would imply simple Larmor precession, in the case of an antisymmetric magnetic slope configuration, this trapping results in mirrored orbits that propagate along the magnetic null in the $+x$-direction (see Figure 3). Thus, for $P_X > 0$, ions will always follow forward-drifting trajectories. We will refer to these trajectories as "linear betatron" (or LB) orbits as per the nomenclature of Jorns and Choueiri.[1]

2. $P_X < 0$

For $P_X < 0$, V_{eff} becomes a symmetric double well with minima on the Y-axis and a maximum at $Y = 0$. To determine ion trajectories for $P_X < 0$, let us first consider the case where $P_X = -7$ and the Hamiltonian $\mathcal{H}_{\bar{r}_L}$ is small (see I in Figure 4). In this case, the ion is trapped in a symmetric well about one of the minima, and exhibits Larmor precession due to the homogeneity of the magnetic field in that region (see trajectory I in Figure 5). These trajectories will be referred to as Larmor orbits.

As the value of $\mathcal{H}_{\bar{r}_L}$ increases, Larmor precession persists until the ion begins to experience asymmetry about the minimum of the well (see II in Figure 4). Physically, this corresponds to the ion just entering the magnetic slope region ($Y < |\bar{\delta}|$). Thus, in this regime, the ion experiences a grad-B drift in its guiding center in the $-x$-direction, but still does not cross the magnetic null (see trajectory II in Figure 5). These trajectories will be referred to as grad-B (or ∇B) orbits.

(a) $P_X = 1$, $\mathcal{H}_{\overline{r}_L} = 10$

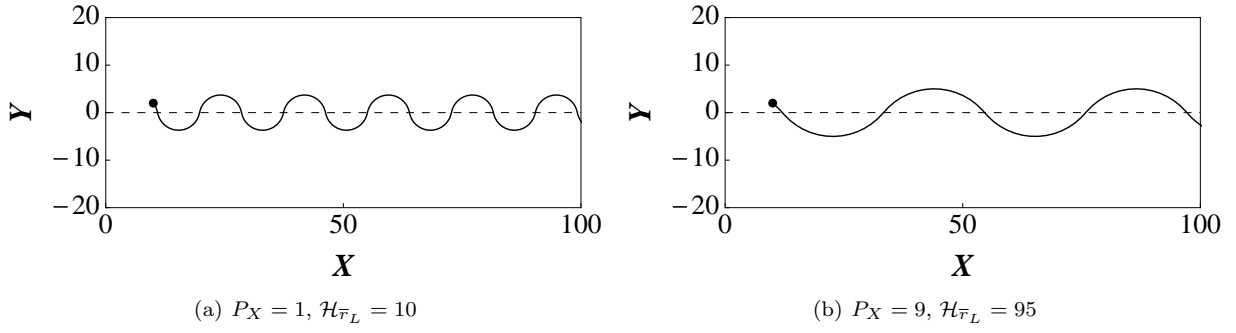(b) $P_X = 9$, $\mathcal{H}_{\overline{r}_L} = 95$

Figure 3. Sample ion trajectories for $P_X > 0$. A black dot is used to show the ion's initial position in each plot. In the LB case, the guiding center of ion motion generally lies across the magnetic null in the region of opposite field polarity. Thus, an ion will never complete more than half of a circular orbit before crossing $Y = 0$. As a result, Y is clearly single-valued in X for LB trajectories.

Increasing $\mathcal{H}_{\overline{r}_L}$ further results in the ion overcoming the potential barrier at $Y = 0$ and actually crossing the magnetic null (see III in Figure 4). For sufficiently low values of $\mathcal{H}_{\overline{r}_L}$, the ion follows a "figure-8" trajectory and experiences a net drift in the $-x$-direction (see trajectory III in Figure 5). These trajectories will be referred to as reverse figure-8 orbits.

As $\mathcal{H}_{\overline{r}_L}$ increases further, ions continue to trace out figure-8 trajectories, but their drift velocities increase until they ultimately experience a net drift in the $+x$-direction (see IV in Figures 4 and 5). Upon even further increases in $\mathcal{H}_{\overline{r}_L}$, these figure-8 trajectories are stretched in X (and Y, but to a lesser extent) and ion motion converges to the LB orbits observed for $P_X > 0$ (see trajectory VI in Figure 5).

3. Orbit Domain Representations

This completes our classification of characteristic ion orbits in the unperturbed case. The regions of P_X-$\mathcal{H}_{\overline{r}_L}$ phase space occupied by each trajectory are depicted graphically in Figure 6(a). However, in order to better intuit the relative frequency of each orbit in a thermalized ensemble, we must recast these orbit domains in terms of more physical variables – namely, the normalized Larmor radius ρ of the ion and the Y-position of its guiding center Y_{GC}. We also introduce a physical boundary in the form of thruster walls and consider only particles whose trajectories fall within the region $|Y| < L$, where L is the thruster half-width in Y. The result of this coordinate transformation is depicted in Figure 6(b).

C. Ensemble Behavior

Next, we consider the behavior of a collisionless ion ensemble subject to the magnetic slope described in Eq. (1). We assume that the initial velocity distribution of such an ensemble is described by a two-dimensional (since only $v_\perp$ is relevant) Maxwell-Boltzmann distribution. In $\overline{r}_L$-normalized coordinates, a 2-D Maxwellian has the following velocity component distribution:

$$f_v(v_i)\, dv_i = f_V(V_i)\, dV_i = \frac{1}{\overline{V}\sqrt{\pi}} \exp\left[-\frac{V_i^2}{\overline{V}^2}\right] dV_i \tag{7}$$

where $V_X = X'$, $V_Y = Y'$, and $\overline{V} = \overline{v}/\omega_{ci}\overline{r}_L$. But $\overline{r}_L = \overline{v}/\omega_{ci}$ by definition and

$$\overline{\rho} = \sqrt{\langle\rho^2\rangle} = \sqrt{\langle V_X^2 + V_Y^2\rangle} = \sqrt{\langle V^2\rangle} = \overline{V}$$

where $\overline{\rho}$ is the normalized RMS Larmor radius of the ensemble and $\langle\ldots\rangle$ denotes the average value. Thus, for a $\overline{r}_L$-normalized ensemble, $\overline{V} = \overline{\rho} = 1$. The velocity distribution can thus be expressed in the following simplified form:

$$f_V(V_i)\, dV_i = \frac{1}{\sqrt{\pi}} \exp\left[-V_i^2\right] dV_i \tag{8}$$

This expression defines a normal distribution of velocity component V_i with a mean value μ of zero and a standard deviation σ of $1/\sqrt{2}$. Initial ion velocities for all subsequent simulations are sampled from this
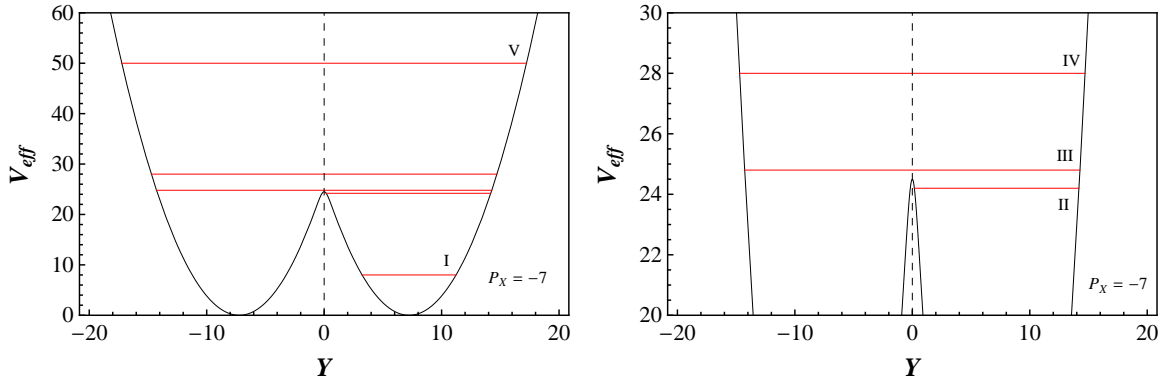
Figure 4. V_{eff} plot for $P_X = -7$. A magnified portion of the same plot is included for clarity. Red lines denote values of $\mathcal{H}_{\overline{r}_L}$ for five test ions. Each line matches up with a corresponding particle trajectory (labeled I-V) featured in Figure 5 below. A particle encounters a turning point (Y-bound) in its orbit whenever its corresponding $\mathcal{H}_{\overline{r}_L}$ line intersects the V_{eff} curve.
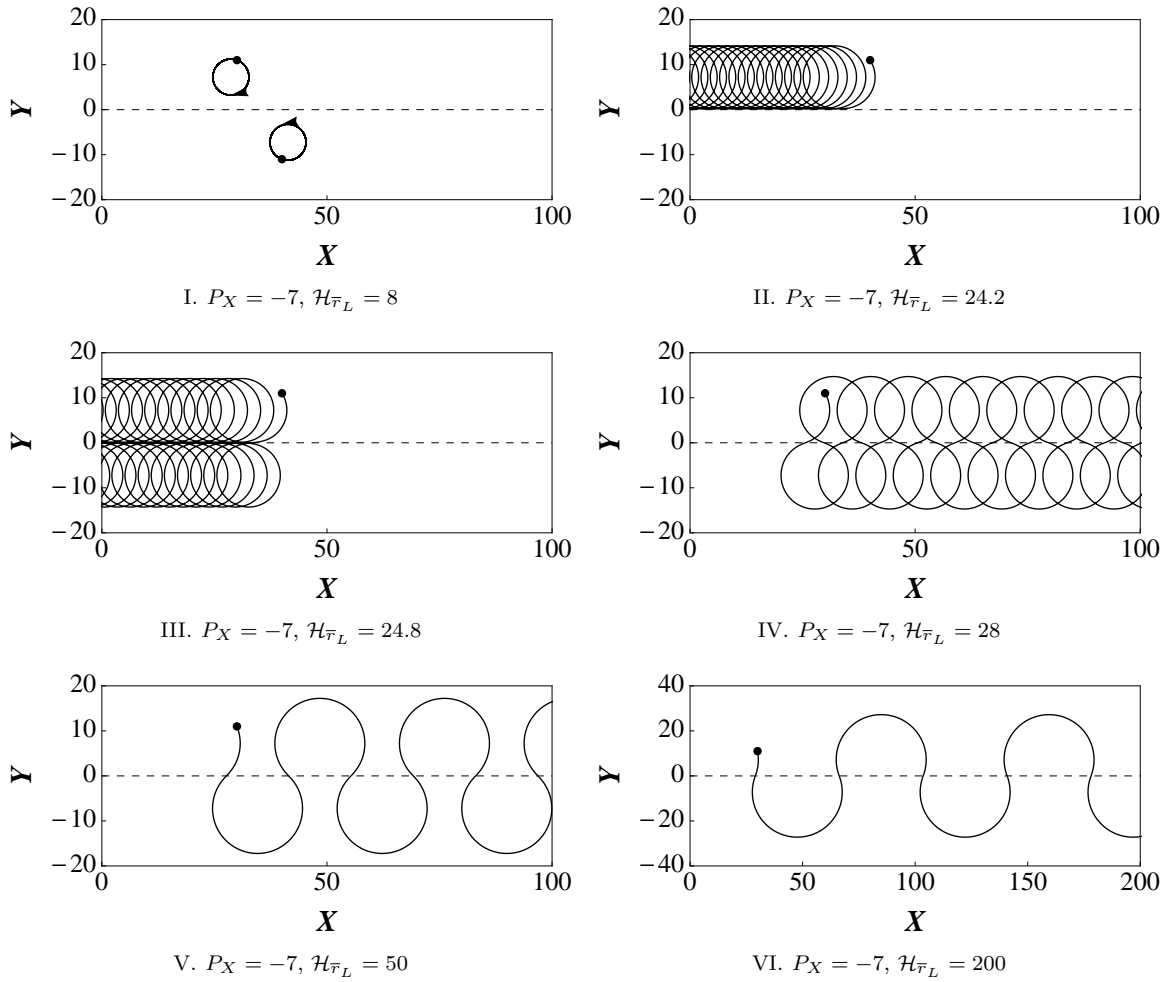

I. $P_X = -7$, $\mathcal{H}_{\overline{r}_L} = 8$

II. $P_X = -7$, $\mathcal{H}_{\overline{r}_L} = 24.2$

III. $P_X = -7$, $\mathcal{H}_{\overline{r}_L} = 24.8$

IV. $P_X = -7$, $\mathcal{H}_{\overline{r}_L} = 28$

V. $P_X = -7$, $\mathcal{H}_{\overline{r}_L} = 50$

VI. $P_X = -7$, $\mathcal{H}_{\overline{r}_L} = 200$

Figure 5. Characteristic ion trajectories for $P_X < 0$. Each trajectory (except **VI**) matches up with a corresponding $\mathcal{H}_{\overline{r}_L}$ value depicted in Figure 4.
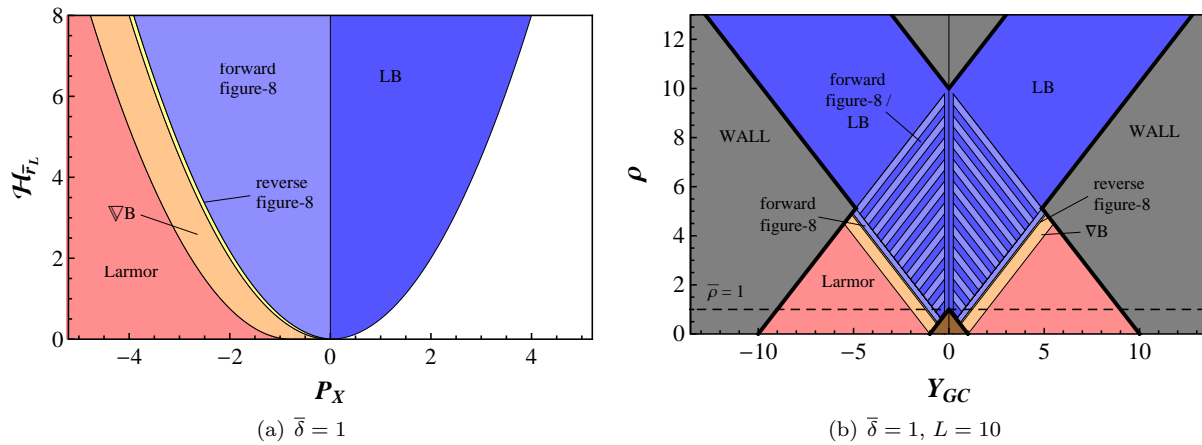
Figure 6. (a) Trajectory classification plot depicting the domains of characteristic ion orbits in the P_X-$\mathcal{H}_{\bar{r}_L}$ plane. The white region is inaccessible to ions due to the inherent structure of the phase space. (b) Region plot depicting characteristic orbit domains in Y_{GC}-ρ space. The brown region is indeterminate by our analysis (since $Y < |\bar{\delta}|$) and the gray regions are inaccessible due to the presence of physical walls (located a distance L from the magnetic null in Y).

distribution. Note that since $\bar{r}_L$ normalization universally maps $\bar{\rho}$ to one, this distribution is fixed; it is a universal Maxwellian that represents a thermalized ion ensemble at an arbitrary temperature. This implies that results from simulations involving $\bar{r}_L$-normalized Hamiltonians are generalizable to all ion temperature values.

A dotted line representing $\bar{\rho} = 1$ is featured in the region plot in Figure 6(b). The relative length of the $\bar{\rho}$ segment that falls within a given orbit domain in ρ-Y_{GC} space yields an intuitive (albeit rough) estimate of the relative prominence of that particular orbit in the context of the entire ensemble. Thus, for $L = 10$, we see that a majority of ions are trapped in Larmor orbits and very few follow forward-drifting trajectories. From the standpoint of thrust generation, this is clearly undesirable. One way to increase the fraction of ions subject to these forward-drifting orbits is to constrict thruster geometry by decreasing L. As L decreases, the number of ions subject to forward-drifting orbits initially increases. However, the fraction of ions that "escape" to the walls also grows with decreasing L. These two conflicting behaviors imply that an optimal L value can be determined such that the percentage of ions subject to forward-drifting orbits is a maximum.

1. L Optimization

In order to determine the optimal thruster geometry, we used a numerical simulation featuring approximately 15,000 ions divided evenly amongst approximately three thousand starting Y positions (such that $\bar{\delta} < |Y_0| < L$, where the subscript $_0$ denotes an initial value) with normalized velocity components randomly selected from the distribution defined in Eq. (8). From these initial conditions, we were able to deduce ρ and Y_{GC} values for each ion. The results of these simulations are featured in Figure 7 in the form of contour plots. Figure 7(a) confirms our initial postulate that for $L = 10$, the vast majority of ions are trapped in Larmor orbits. Figure 7(b), however, depicts the optimal thruster geometry ($L \approx 1.6$) for a collisionless, $\bar{r}_L$-normalized ion ensemble. Numerical results reveal that for this optimized system, the fraction of forward-drifting ions ξ_f is approximately 34.9% while the fraction of ions that escape to the walls ξ_{esc} is approximately 53.5%. The remaining ions (11.6%) follow either reverse-drifting or Larmor trajectories. Furthermore, the fixed nature of $\bar{\rho}$ in the context of this simulation means that this geometric configuration essentially represents the universal optimum for every thermalized distribution of ions subject to a steeply-sloped z-directed magnetic field.

2. Benchmark Specific Impulse

Next, we sought to determine a theoretical specific impulse value for our L-optimized thruster geometry. Only forward-drifting ions were considered (including, for completeness, ions that started in the sloped region). We also assumed that ions lost to the walls did not contribute to the exhaust plume. To determine the exhaust velocity, we concentrated our ensemble in a very small X-range (~ 0.1) and specified an arbitrary
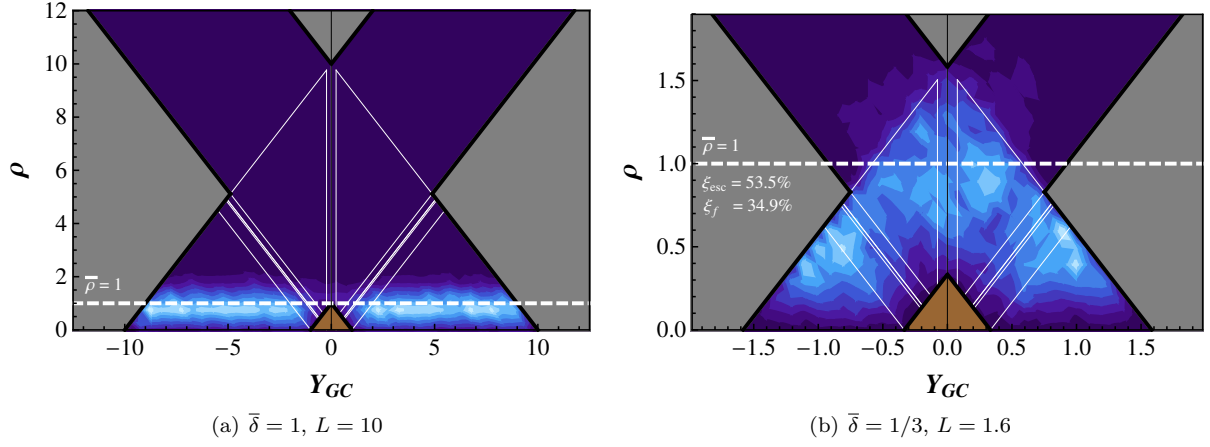
(a) $\bar{\delta} = 1$, $L = 10$ (b) $\bar{\delta} = 1/3$, $L = 1.6$

Figure 7. (a) Contour plot of a 2-D Maxwellian velocity distribution in the ρ-Y_{GC} plane subject to the constraints of thruster geometry. White lines are used to delimit the orbit domains featured in 6(b). Lighter regions indicate greater particle density. (b) Contour plot depicting the optimal thruster geometry for a $\bar{r}_L$-normalized ion ensemble.
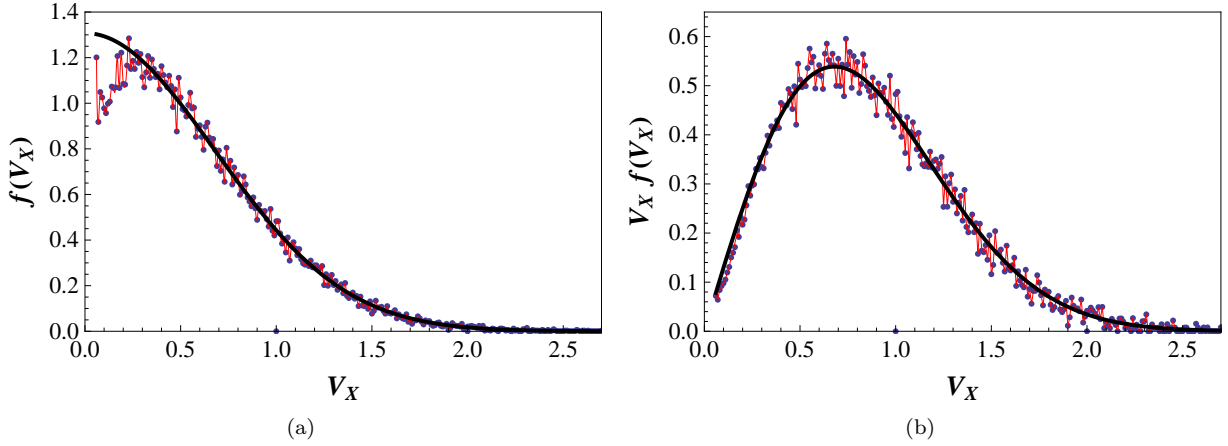

(a)   (b)

Figure 8. (a) Average exit velocity distribution. The black curve is a a half-Gaussian best fit. (b) A plot of the product of exit velocity and the distribution $f(V_X)$. The integral of the resulting curve is the average exit velocity, or the (normalized) exhaust velocity U_{ex}.

plane in X that we defined as the exit plane. An ion that breaks this plane is considered part of the exhaust plume, and the average velocity V_X at which it does so is considered to be the exit velocity of the ion. As expected, the exhaust velocity of the thruster is defined as the average velocity of the exhaust plume.

Figure 8(a) depicts the exit velocity distribution for a sample size of approximately 10,000 ions. This plot unambiguously demonstrates that the magnetic slope configuration can indeed produce a net linear ion current in the X-direction. The distribution can be approximated by a half-Gaussian, which agrees very well with numerical results for large V_X. But for small V_X, numerical results clearly diverge from the fit. While this could indeed be a characteristic of the thruster itself (which is likely given that this drop-off was observed even for very large time intervals), it could also be a result of the drawbacks of our chosen method. However, seeing as the exhaust velocity is defined such that

$$U_{ex} = \int_0^\infty V_X f(V_X)\, dV_X \tag{9}$$

and noting the improved correlation of the transformed fit in Figure 8(b), we conclude that for the purposes of exhaust velocity calculations, the half-Gaussian approximation is acceptable.

This simulation ultimately yielded a normalized exhaust velocity U_{ex} of 0.6. In other words, in this optimized geometry in the unperturbed case, the average exiting ion enters the exhaust plume with an

X-velocity equal to 60% of the average initial perpendicular velocity of the ensemble.

From this normalized exhaust velocity value, we use realistic physical parameters to calculate the benchmark I_{sp} for the optimal unperturbed thruster configuration. By definition,

$$U_{ex} = \frac{u_{ex}}{\bar{v}} \tag{10}$$

where $\bar{v}$ is the RMS velocity of the 2-D ensemble. Also by definition (for a Maxwellian),

$$\bar{v} = \sqrt{\frac{2k_B T_i}{m}} \tag{11}$$

where k_B is Boltzmann's constant, T_i is the temperature of the ion ensemble, and m is the ion mass. Thus, by specifying an ion temperature T_i and recalling that $I_{sp} = u_{ex}/g_0$, we can determine u_{ex} for an ensemble of ions each with mass m.

For example, consider an ensemble of hydrogen ions ($m \approx 1.67 \times 10^{-27}$ kg) with an average temperature of $T_i = 0.1$ eV. For $g_0 = 9.81$ m/s^2, this yields a theoretical I_{sp} of approximately 270 s. For an ensemble of argon ions ($m \approx 6.63 \times 10^{-26}$ kg), this theoretical I_{sp} drops precipitously to about 40 s.

3.   Benchmark Thrust Density

Next we use the average exhaust velocity distribution to determine an approximate expression for the thrust generated by this magnetic slope configuration. Recall that

$$\mathbf{T} = \dot{m}\mathbf{u}_{ex} \tag{12}$$

By assuming that these two quantities are not independent, we can approximate the $\dot{m}$ term as follows:

$$\dot{m} = nm\xi_f A u_{ex} = 2nm\xi_f \bar{r}_L L_{max} \ell u_{ex} \tag{13}$$

where A is the cross-sectional area of the thruster, ℓ is the depth of the thruster in the z-direction, n is the average ion density, and m is the ion mass. The inclusion of ξ_f accounts for the fact that only forward drifting ions contribute to the mass flow from the thruster. Thus, we can approximate the thrust generated per unit thruster depth (in z) in terms of fundamental physical parameters as follows:

$$\frac{T}{\ell} = 2nm\xi_f \bar{r}_L L_{max} u_{ex}^2 = 2^{5/2} \left(\xi_f L_{max} U_{ex}^2 \right) \frac{n\sqrt{m}(k_B T_i)^{3/2}}{qB_0} \tag{14}$$

We see from the above expression that we can change the thrust of the unperturbed optimized configuration for a given plasma via the manipulation of three parameters: n, T_i, and B_0. However, this expression is only an approximation, and considers neither the mechanism by which thrust is actually transferred to the spacecraft nor the complex particle interactions that are often characteristic of plasma behavior. Nevertheless, it should still provide a somewhat reasonable estimate for the expected thrust level of a given configuration. Even if the actual values it produces turn out to be inaccurate, the expression can still be used to gauge the relative thrust levels of comparable configurations.

In calculating hypothetical thrust values, we used data collected by Jorns and Choueiri in 2010 from the second-generation Beating Wave Experiment (BWXII).[8] Thus, for a singly-ionized argon plasma with $n \approx 10^{10}$ cm^{-3} and $T_i \approx 0.1$ eV in a B-field of 500 Gauss, the calculated linear thrust density is approximately 7.4×10^{-7} N/m – an incredibly small result. For a hydrogen plasma of equal density and temperature, the thrust density is even lower: $T/\ell \approx 1.2 \times 10^{-7}$ N/m.

D.   Performance Assessment

The specific impulse values calculated in the previous section are remarkably low for electric thrusters. However, given the fact that in the unperturbed case, the Hamiltonian of each individual ion is conserved, these results are unsurprising. In its current form, this magnetic field configuration essentially takes the thermal energy of an ion ensemble and concentrates a portion of it in the $+X$-direction, establishing a linear ion current along the magnetic null. If the thruster were 100% efficient, it would concentrate 100% of that thermal energy such that $U_{ex} \approx 1$. Thus, in its current configuration (and for the specified ion temperature), the maximum I_{sp} (assuming $U_{ex} = 1$) for a hydrogen thruster of this type is only about 450 s (for an argon

thruster it is approximately 70 s). Much of the same reasoning applies to why the calculated thrust values are also very low.

In their seminal paper that introduced this propulsion concept, Jorns and Choueiri proposed that BEW propagation would augment the linear ion current generated along the magnetic null.[1] In the interest of demonstrating the enhancement of both current flow and current density along the null (and thereby increasing both the net thrust and I_{sp} of the thruster), in the next section we consider the perturbed case ($\varepsilon \neq 0$) and investigate the effects that beating waves have on the propulsive characteristics of this sloped field configuration.

III.   Effects of BEW Propagation

A.   BEW Phenomenon

Before immediately delving into the perturbed case, we must first elucidate the basic physics of BEW acceleration, as well as its propulsive applications.

Background

In 1998, Ram *et al* proposed that particle interactions with a spectrum of electrostatic ion cyclotron (EIC) waves propagating perpendicularly to the Earth's magnetic field were responsible for the prodigious ion acceleration observed in the upper ionosphere.[9] In that same year, Benisti *et al* theoretically demonstrated that ions with arbitrarily low initial velocities can be stochastically accelerated via nonlinear wave-particle interactions if the aforementioned electrostatic spectrum contains at least two waves that satisfy a mathematical "beating criterion" such that their frequencies differ by an integer multiple of the cyclotron frequency:[10, 11]

$$\omega_2 - \omega_1 = \alpha\,\omega_{ci} \tag{15}$$

where ω_1 and ω_2 are the wave frequencies, $\omega_{ci} = qB/m$ is the local ion cyclotron frequency, and α is a nonzero integer.

In 2004, Spektor and Choueiri showed that although the beating criterion is necessary for such acceleration to occur, it is not sufficient.[12] They determined that low-velocity ions are accelerated only if their initial Hamiltonians fall within a specific range. However, in spite of this restriction, BEW propagation still results in the acceleration of ions with initial velocities well below the phase velocities of the exciting waves. This stands in stark contrast to single electrostatic wave (SEW) acceleration, in which only the portion of the ion distribution that satisfies a broadened resonance condition experiences stochastic acceleration. This implies that for a general distribution, a larger portion of ions will satisfy the less stringent BEW acceleration criteria than will satisfy the corresponding SEW resonance condition.

Ion heating via BEW propagation was first demonstrated in a laboratory setting by Spektor and Choueiri in 2005.[13] In 2009, Jorns and Choueiri were able to unambiguously demonstrate the superiority of BEW heating over SEW heating.[14] They reported a 90% increase in perpendicular ion temperature for BEW heating versus only a 50% increase for SEW heating at comparable wave energy densities. In 2011, Jorns and Choueiri derived an analytical expression that demonstrated the superiority of BEW heating over SEW heating for all parameter space.[15] This claim was also confirmed by their numerical results.

Hamiltonian Formulation and Analysis

After normalizing length to k^{-1} and time to ω_{ci}^{-1}, the Hamiltonian of an ion in a uniform magnetic field subject to a spectrum of perpendicularly propagating electrostatic waves takes the following action-angle form:

$$\overline{\mathcal{H}}_k = \frac{\rho^2}{2} + \varepsilon \sum_{i=1}^{n} \cos\left(\rho\sin\theta - \nu_i\tau\right) \tag{16}$$

where ρ is the normalized Larmor radius, θ is the Larmor phase angle, ε is the normalized wave amplitude, ν_i is the normalized frequency, and τ is a normalized time variable ($\tau = \omega_{ci}t$). In the BEW case, $n = 2$ and the wave frequencies ν_1 and ν_2 satisfy the normalized beating criterion such that $\nu_2 - \nu_1 = \alpha$. In the SEW case, of course, $n = 1$.

(a) SEW ($\varepsilon = 10$, $\nu = 24.3$)　　　　　　　　(b) BEW ($\varepsilon = 10/\sqrt{2}$, $\nu_1 = 24.3$)
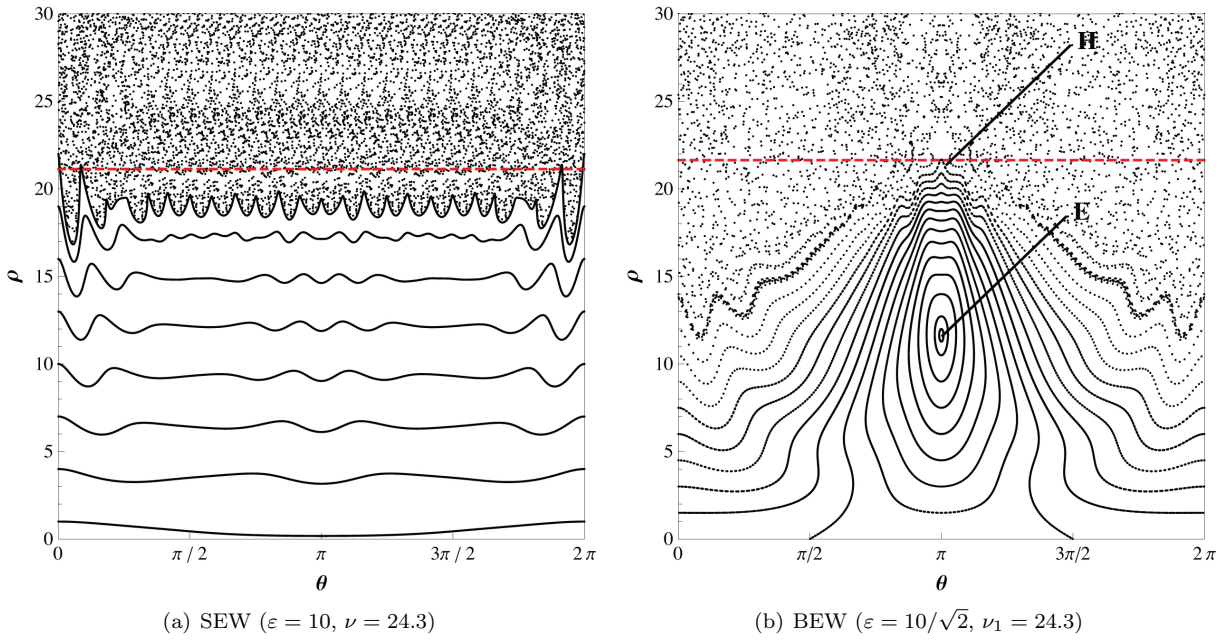
Figure 9. Poincaré sections for the off-resonant (a) SEW ($\varepsilon = 10$, $\nu = 24.3$) and (b) BEW ($\varepsilon = 10/\sqrt{2}$, $\nu_1 = 24.3$) cases. Each section is a projection of ion motion onto the (ρ, θ) plane at a fixed interval τ_c corresponding to either (a) the normalized period of the exciting wave ($2\pi/\nu$) or (b) the least common period of the beating waves. Each well-defined curve represents the trajectory of a single test ion in phase space. Normalized amplitudes were chosen such that total wave energy density is equal in both cases. In both plots, the dashed red line represents the single-wave stochastic threshold. In the BEW case, the hyperbolic and elliptic points are labeled H and E, respectively.

Because Hamilton's equations reveal that this nonlinear system has no general closed-form solution, we turn to Poincaré sections to gain greater physical insight into ion behavior in the SEW and BEW cases. Figure 9(a) is a typical Poincaré section for an ion subject to a SEW. Karney determined that in order for an ion to experience SEW acceleration, the ion's velocity must fall within a certain range, thereby satisfying a broadened resonance condition.[16] The dashed red line depicts the lower bound of said range. This stochastic threshold is analytically defined as follows:

$$\rho_{th} \equiv \nu - \sqrt{\varepsilon} \tag{17}$$

Figure 9(a) reveals that ion motion is coherent for $\rho \lesssim \rho_{th}$ and stochastic for $\rho \gtrsim \rho_{th}$. Thus, phase space for a magnetized ion subject to a SEW can be divided into two distinct regions of ion motion: a *forbidden* region, where wave-ion interactions are small and ion motion is coherent, and a *stochastic* region, where wave-ion interactions are strong and ion motion is effectively chaotic. In the SEW case, these coherent and stochastic regions of phase space remain strictly separate. If an ion starts in a given regime, it remains in said regime for all time. As such, only ions with $\rho \gtrsim \rho_{th}$ exchange energy with the exciting wave; low-velocity ions are not appreciably accelerated.

For comparison, Figure 9(b) features a Poincaré section of ion phase space in the BEW case. The corresponding SEW stochastic threshold is included for reference. Normalized beating wave amplitudes were chosen such that total wave energy densities are equal for both cases depicted in Figure 9. We see from the BEW plot that contrary to the SEW case, ions subject to BEW can experience appreciable coherent acceleration. This coherent acceleration is observed in two forms: either the ion is coherently accelerated up to the stochastic threshold, after which it enters the chaotic regime (somewhere in the vicinity of the hyperbolic point **H**) and is subsequently stochastically accelerated, or it is coherently accelerated up to a maximum $\rho_{max} < \rho_{th}$ and then coherently decelerated. While the first case corresponds to a gradual and subsequently chaotic increase in Larmor radius ("regular acceleration"), the second corresponds to the periodic contraction and expansion of a magnetized ion's orbit about its guiding center ("forbidden acceleration"). Thus, BEW phase space can be divided into three regimes: the forbidden acceleration region, the regular acceleration
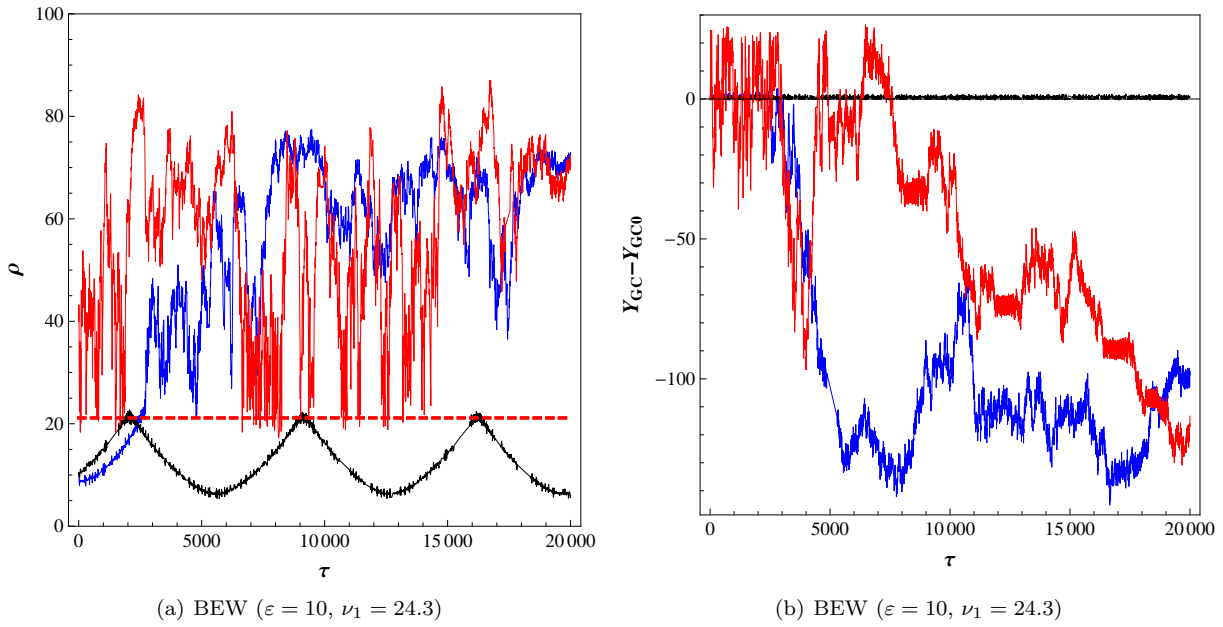
(a) BEW ($\varepsilon = 10$, $\nu_1 = 24.3$)   (b) BEW ($\varepsilon = 10$, $\nu_1 = 24.3$)

Figure 10. **Time evolution of (a) ρ and (b) Y_{GC} in the off-resonant BEW case ($\varepsilon = 10$, $\nu_1 = 24.3$) for various initial conditions (ρ_0 and θ_0). The dotted red line represents the SEW stochastic threshold ρ_{th}. Note that stochastic acceleration results in a net displacement of the guiding center in the $\mathbf{k} \times \mathbf{B}$ direction.**

region, and the stochastic acceleration region. While in the SEW case the stochastic and coherent regions are strictly separate, in the BEW case, they are connected via the regular acceleration region. As a result, an ion with very low initial velocity can be coherently accelerated up to and through the stochastic threshold. Thus, the broadened resonance characteristic of SEW acceleration is clearly not required for significant BEW acceleration to occur.

Note that the stochastic threshold described in (17) decreases with decreasing frequency and increasing wave amplitude. For a general distribution, a decrease in the stochastic threshold results in an increase in the number of ions subject to acceleration. This is true for both SEW and BEW acceleration.

Figure 10 features the time evolution of ρ and $Y_{GC} - Y_{GC0}$ (the normalized Y-displacement of the guiding center, where $Y = ky$) for three test ions. The black curve represents an ion in the forbidden acceleration region. The ion is coherently accelerated and decelerated periodically as its Larmor radius oscillates between ρ_{th} and some minimum value. The ion's guiding center remains fixed in Y (aside from ignorable fluctuations) for all time. The red curve represents an ion that starts in the stochastic region such that $\rho_0 > \rho_{th}$. The ion experiences appreciable energization as its Larmor radius oscillates stochastically in the region above ρ_{th}. Over time, the guiding center of the ion experiences a net drift in the $\mathbf{k} \times \mathbf{B}$ direction (in this configuration, the negative Y direction). Finally, the blue curve represents an ion that starts in the regular acceleration regime and is coherently accelerated through the stochastic threshold. This curve in particular illustrates the principal benefit of BEW over SEW: despite ρ_0 being less than half of ρ_{th}, the stochastic regime is clearly still accessible to the ion. Furthermore, while the ion's guiding center remains fixed during the coherent portion of the acceleration, upon stochastic energization it too experiences a clear negative displacement in Y_{GC}.

Propulsive Applications

As aforementioned, Jorns and Choueiri have demonstrated both analytically and experimentally that BEW propagation is a comparatively efficient method for heating a plasma. Thus, the BEW phenomenon clearly has potential applications in the heating stage of an electrothermal thruster.

In this paper, however, we seek to demonstrate the feasibility of a propulsion concept that exploits the direct acceleration of individual ions via BEW (as opposed to ensemble heating and subsequent expansion through a suitable nozzle). As previously demonstrated, the physical manifestation of BEW acceleration is an increase in the Larmor radius of the ion. In this section, since our thruster operates via the conversion

of gyromotion to linear motion, we seek to demonstrate that radial BEW acceleration enhances thruster performance by increasing both the speed and density of ions flowing along the magnetic null. Furthermore, we also show that the stochastic drift of the guiding center in the $\mathbf{k} \times \mathbf{B}$ direction may help to minimize wall losses in the context of an actual thruster geometry. And finally, since the properties of BEW acceleration clearly change with the variation of wave parameters, we expect BWT performance characteristics to change in a related fashion, thereby implying thruster variability.

B.   Perturbed Ion Dynamics

Recall that the $\overline{r}_L$-normalized BEW Hamiltonian is

$$\mathcal{H}_{\overline{r}_L} = \frac{1}{2}\left(\left[P_X - \overline{A}_X\right]^2 + P_Y^2\right) + \frac{\varepsilon}{\kappa}\sum_{i=1}^{2}\cos(\kappa X - \nu_i \tau) \tag{18}$$

where ν_1 and ν_2 satisfy the beating criterion. The goal of subsequent analysis is to determine how BEW propagation alters the orbits of unperturbed ions.

Following the convention of Jorns and Choueiri,[1] we partition our analysis by grouping ions based on the relationship between the initial Y-position of the guiding center Y_{GC0}, the initial normalized Larmor radius ρ_0, and the stochastic threshold for BEW acceleration ρ_{th}. Note that while the k-normalized stochastic threshold was previously defined as $\rho_{th} = \nu - \sqrt{\varepsilon}$, $\overline{r}_L$ normalization yields a slightly different expression due to the presence of an additional parameter κ:[15]

$$\rho_{th} = \frac{\nu}{\kappa} - \sqrt{\frac{\varepsilon}{\kappa}} \tag{19}$$

First, we group unperturbed ions into two categories: a forward-drifting category (which includes forward figure-8 and LB trajectories) and a non-forward-drifting category (which includes reverse figure-8, grad-B, and Larmor trajectories). A given unperturbed ion will only follow a forward-drifting trajectory if $\rho_0 > \rho_f$, where

$$\rho_f \approx |Y_{GC0}| \tag{20}$$

Next, we treat four relevant cases of motion based on the initial conditions of a given ion (more specifically, the relationship between ρ_0, ρ_f, and ρ_{th}).

Case 1: $\rho_0 < \rho_f < \rho_{th}$

In the case where $\rho_0 < \rho_f < \rho_{th}$, the ion starts in the non-forward-drifting regime, and the Larmor radius at which it enters the forward-drifting regime is *below* the stochastic threshold for BEW acceleration.

Figure 11 depicts the time evolution of ρ and $\rho_f - \rho$ for a test ion subject to BEW that satisfies $\rho_0 < \rho_f < \rho_{th}$. The sign of $\rho_f - \rho$ determines the drift behavior of the ion. For $\rho_f - \rho > 0$, the Larmor radius of the ion is less than the Larmor radius required to enter the forward-drifting region; therefore, the ion follows a non-forward-drifting trajectory. For $\rho_f - \rho < 0$, the ion's gyroradius is greater than the Larmor radius required for the ion to enter the forward-drifting regime; thus, the ion follows a forward-drifting trajectory.

Figure 11(a) shows that for $\rho_0 < \rho_f < \rho_{th}$, the test ion coherently accelerates up to ρ_f, but immediately decelerates upon encountering the magnetic null. Figure 11(b) depicts the same behavior: the ion coherently approaches the forward-drifting region, but is deflected upon reaching the $\rho_f - \rho = 0$ barrier. While numerical results have shown that this does not necessarily prevent the ion from entering the forward-drifting regime, it *does* prevent the ion from remaining in the forward-drifting regime for appreciable periods of time (i.e. more than a few Larmor orbits). These ions tend to experience periodic kicks in X_{GC} that are too small and infrequent to be considered forward-drifting. Thus, we conclude that on the whole, ions initially in non-forward-drifting orbits *cannot* be coherently accelerated into the forward-drifting regime.

Case 2: $\rho_0 < \rho_{th} < \rho_f$

For $\rho_0 < \rho_{th} < \rho_f$, the ion clearly starts outside the forward-drifting regime, and the Larmor radius at which it enters said regime is *above* the BEW stochastic threshold.
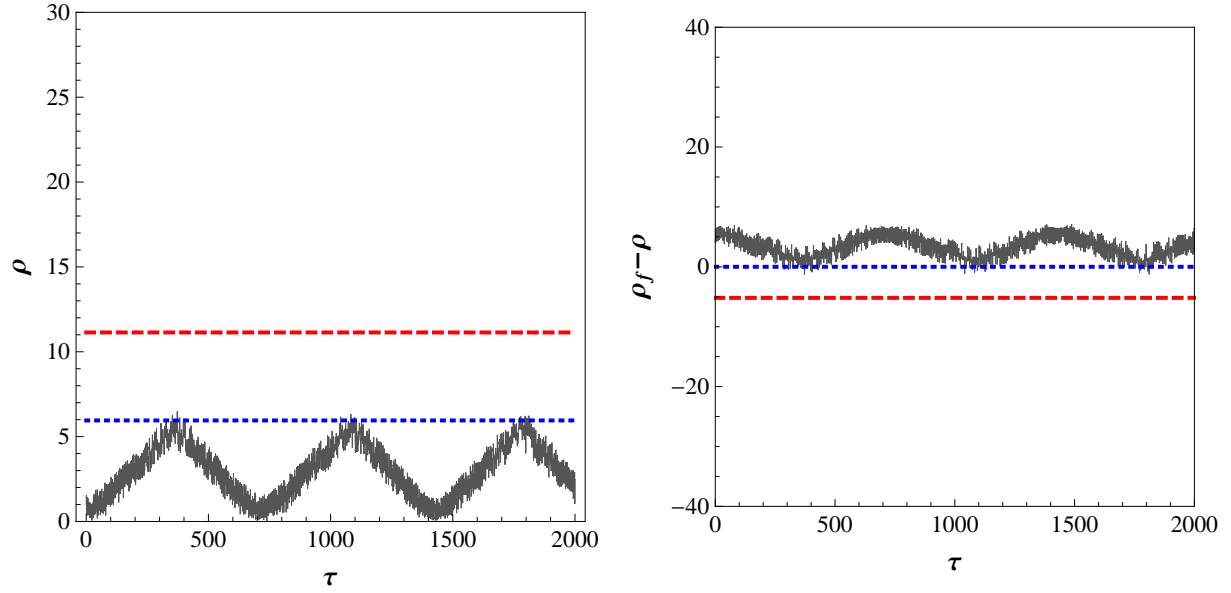
(a) Time evolution of ρ (gray). The dotted blue line represents ρ_f; the dashed red line represents ρ_{th}.

(b) Time evolution of $\rho_f - \rho$ (gray). The dotted blue line represents the boundary between forward-drifting and non-forward-drifting trajectories; the dashed red line represents the stochastic threshold ($\rho_f - \rho_{th}$).

Figure 11. Time evolution of (a) ρ and (b) $\rho_f - \rho$ for $\rho_0 < \rho_f < \rho_{th}$ (wave parameters: $\varepsilon = 10$, $\nu_1 = 14.3$, and $\kappa = 1$).
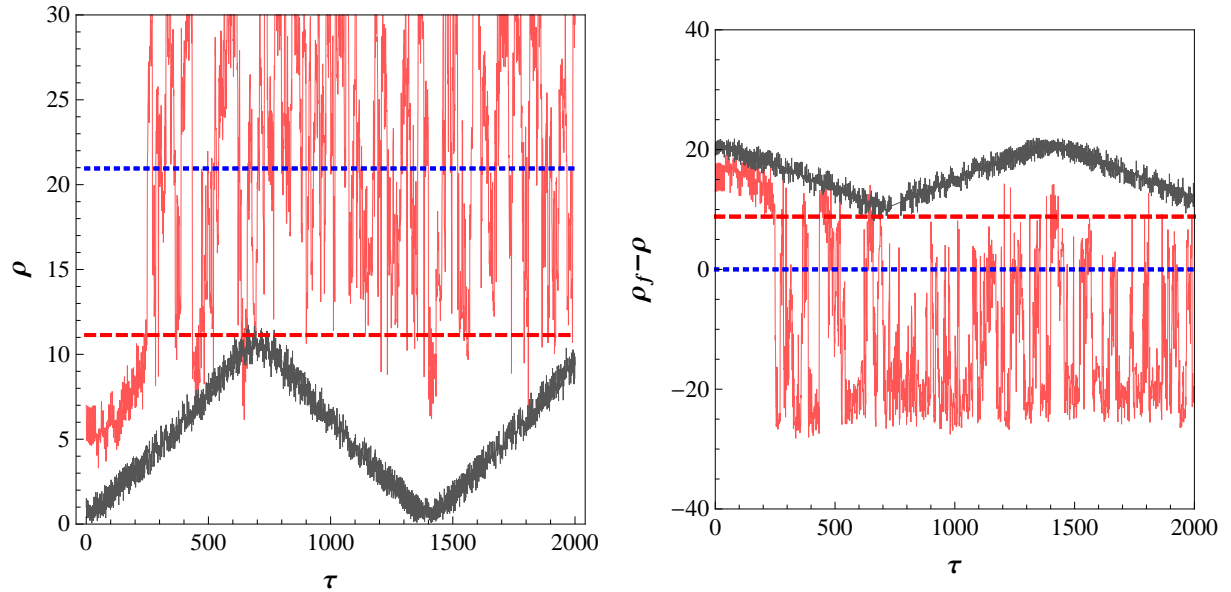

(a) Time evolution of ρ. The dotted blue line represents ρ_f; the dashed red line represents ρ_{th}.

(b) Time evolution of $\rho_f - \rho$. The dotted blue line represents the boundary between forward-drifting and non-forward-drifting trajectories; the dashed red line represents the stochastic threshold ($\rho_f - \rho_{th}$).

Figure 12. Time evolution of (a) ρ and (b) $\rho_f - \rho$ for $\rho_0 < \rho_{th} < \rho_f$ (wave parameters: $\varepsilon = 10$, $\nu_1 = 14.3$, and $\kappa = 1$). The gray curves represent an ion in the forbidden acceleration region; the red curves represent an ion that starts in the regular acceleration region.

The gray curve in Figure 12(a) represents an ion that starts in the forbidden acceleration region. As expected, the ion coherently accelerates up to the stochastic threshold ρ_{th} and then decelerates, never reaching the forward-drifting regime. The red curve, however, represents an ion that begins in the regular acceleration region. This ion is coherently accelerated up to the threshold ρ_{th} where it is then stochastically accelerated into the forward-drifting regime (where it remains, on average; see Figure 12(b)). Thus, for $\rho_0 < \rho_{th} < \rho_f$, BEW propagation can clearly push an ion into the forward-drifting regime as long as it begins in the regular acceleration region. To simplify our analysis, we make the same approximation as Jorns and Choueiri and assume that on average (over θ) ions with $\rho_0 > \rho_{th}/2$ (i.e. ρ above the elliptic point $\mathbf{E}$) are subject to regular acceleration.[1] Thus, we define our first criterion for non-forward-drifting ions to be pushed into the forward-drifting regime:

$$\frac{\rho_{th}}{2} < \rho_0 < \rho_{th} < \rho_f \tag{21}$$

Case 3: $\rho_{th} < \rho_0 < \rho_f$

In the case where $\rho_{th} < \rho_0 < \rho_f$, the ion begins outside the forward-drifting regime, but its initial Larmor radius places it in the stochastic acceleration region.

Figure 13 clearly illustrates that this ion is stochastically accelerated from the outset and promptly enters the forward-drifting regime, where it remains on average for all time. Thus, we can generalize (21) to all ions with $\rho_0 < \rho_f$ as follows:

$$\frac{\rho_{th}}{2} < \rho_0 < \rho_f \tag{22}$$

This expression defines the conditions under which an ion initially following a non-forward-drifting trajectory can be pushed into the forward-drifting region. Thus, the magnitude of ρ_{th} essentially determines the fraction of the reverse-drifting and Larmor populations that can be linearly accelerated along the magnetic null. The smaller the magnitude of ρ_{th}, the greater the number of ions in a given thermalized distribution that can be pushed into forward-drifting trajectories.

Case 4: $\rho_0 > \rho_f$

The final case considers the possibility that ions initially in the forward-drifting region may be pushed into non-forward-drifting orbits as a result of BEW propagation.

Numerical results indicate that these initially forward-drifting ions tend to remain in the forward-drifting region even after BEW perturbation. However, the manner in which their trajectories propagate in X tends to change based on the magnitude of ρ_0 relative to ρ_{th}.

As one might expect, ions with $\rho_0 > \rho_{th}$ tend to stochastically accelerate as they drift forward in X (see Figure 14(a)). As a consequence of this stochastic acceleration, their resultant perturbed X velocities tend to be much higher than their originally-unperturbed counterparts. The blue curves in Figure 14(b) demonstrate this velocity shift. While the dashed blue line represents the unperturbed X trajectory, the solid blue line represents the corresponding perturbed X trajectory. The plot clearly demonstrates that the X velocity of the ion (i.e. the slope of the corresponding blue curve) jumps after the application of BEW.

For $\rho_0 < \rho_{th}$, however, forward-drifting ions tend not to accelerate at all (see Figure 14(a)). The only exception occurs when ions are in the immediate vicinity of ρ_{th}. These ions do tend to undergo regular acceleration and subsequently jump into the stochastic regime. However, aside from this limited range of ρ_0 values near the stochastic threshold, most forward-drifting ions actually exhibit an appreciable *decrease* in X velocity upon encountering BEW. Figure 14(b) illustrates this substantial decrease in velocity for a test ion with $\rho_f < \rho_0 < \rho_{th}$ upon BEW propagation.

Therefore, not only does lowering ρ_{th} effectively increase the number of trapped ions that can be pushed into the forward-drifting region for a given distribution, but it also greatly enhances the flow of ions that were already following forward-drifting trajectories prior to BEW propagation. Thus, we can conclude that by decreasing the magnitude of ρ_{th}, it is likely that we can also dramatically improve the performance of the BWT.
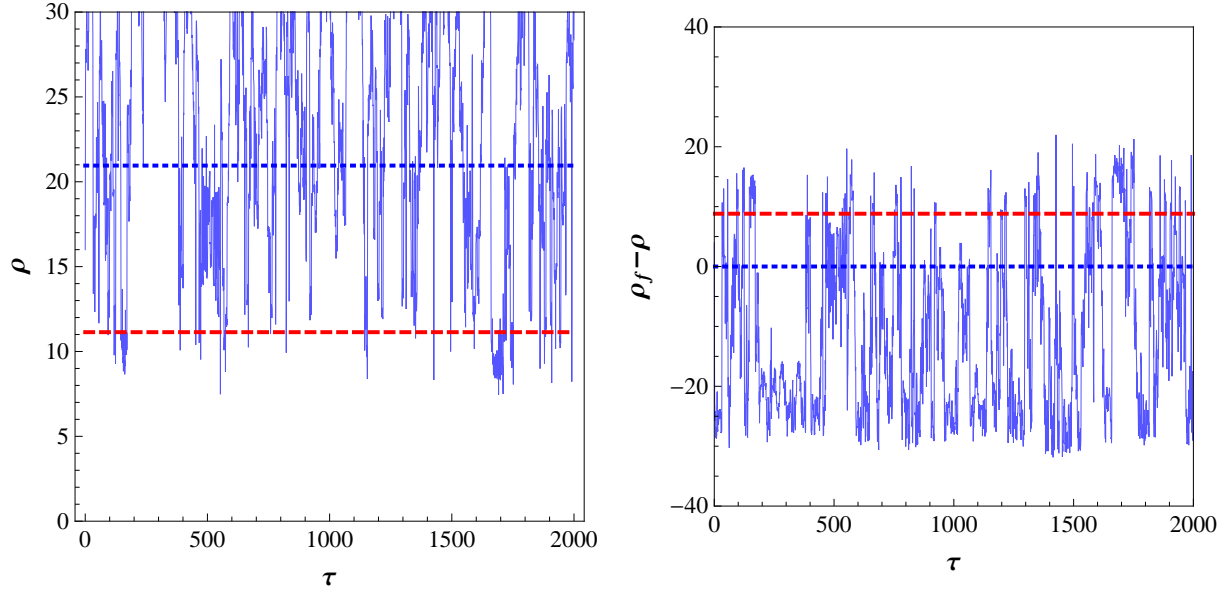
(a) Time evolution of ρ. The dotted blue line represents ρ_f; the dashed red line represents ρ_{th}.

(b) Time evolution of $\rho_f - \rho$. The dotted blue line represents the boundary between forward-drifting and non-forward-drifting trajectories; the dashed red line represents the stochastic threshold $(\rho_f - \rho_{th})$.

Figure 13. Time evolution of (a) ρ and (b) $\rho_f - \rho$ for $\rho_{th} < \rho_0 < \rho_f$ (wave parameters: $\varepsilon = 10$, $\nu_1 = 14.3$, and $\kappa = 1$). The gray curves represent an ion in the forbidden acceleration region; the blue curves represent an ion that starts in the stochastic acceleration region.
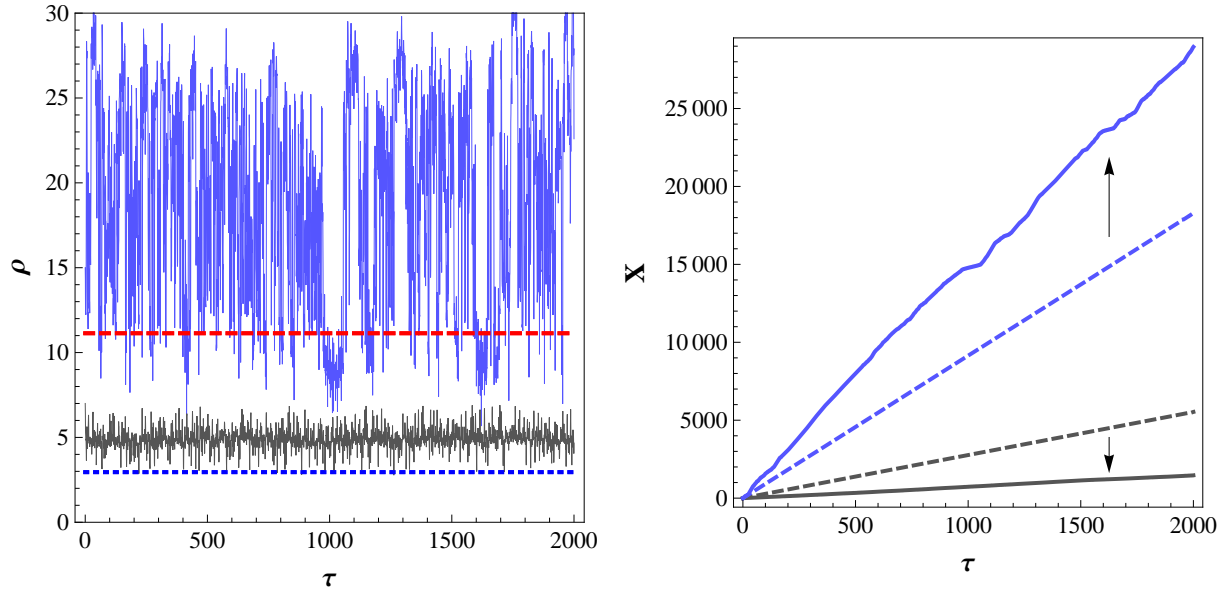
(a) Time evolution of ρ. The dotted blue line represents ρ_f; the dashed red line represents ρ_{th}.

(b) Time evolution of X. Dashed lines represent unperturbed trajectories; solid lines represent perturbed trajectories. The X velocity of an ion is defined as the slope of its corresponding curve.

Figure 14. Time evolution of (a) ρ and (b) X for $\rho_f < \rho_0 < \rho_{th}$ (gray) and $\rho_f < \rho_{th} < \rho_0$ (blue) for wave parameters $\varepsilon = 10$, $\nu_1 = 14.3$, and $\kappa = 1$).
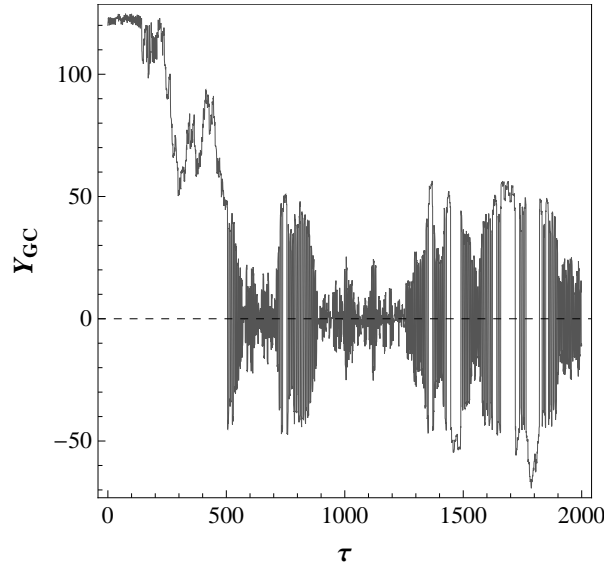
Figure 15. Time evolution of Y_{GC} for a test ion in the regular acceleration regime ($\varepsilon = 10$, $\nu_1 = 14.3$, and $\kappa = 1$). Dense regions about the magnetic null are characteristic of forward-drifting trajectories, in which the guiding center switches sign each time the ion crosses $Y = 0$.

C. Ion Channeling

BEW propagation also has a visible benefit in the context of electric propulsion due to the tendency of guiding centers to drift in the $\mathbf{k} \times \mathbf{B}$ direction after the onset of stochasticity. In the context of this sloped field configuration, this implies that ions in the stochastic region will actually be siphoned towards the magnetic null, a phenomenon which we will henceforth refer to as "ion channeling."

Figure 15 illustrates this phenomenon for a test ion in the regular acceleration region. We see that Y_{GC} remains roughly constant while the ion coherently accelerates. Upon breach of the stochastic threshold, however, the guiding center drops precipitously in Y and gravitates towards the magnetic null, after which it enters the forward-drifting region and the average value of Y_{GC} approaches zero.

Numerical results indicate that ions subject to SEW experience a similar $\mathbf{k} \times \mathbf{B}$ drift in their guiding centers. However, since the stochastic regime is accessible to a larger portion of the ion population in the beating wave case, we expect the channeling effect to be generally more prominent for BEW than for SEW.

This channeling behavior is important from a propulsion standpoint because it implies a net stochastic transport of particles towards the magnetic null, and therefore away from the thruster walls. This effect therefore helps to mitigate characteristic wall losses that hinder the performance of many existing electric thrusters.

D. BWT Performance

1. EIC Dispersion Relation

According to the definition of ρ_{th}

$$\rho_{th} = \frac{\nu}{\kappa} - \sqrt{\frac{\varepsilon}{\kappa}}. \tag{23}$$

We can make the stochastic threshold arbitrarily small by manipulating the parameters ε, ν, and κ as we please. However, this notion of arbitrary manipulation of wave parameters is unphysical in that it neglects the actual behavior of EIC waves in a plasma. The first problem is that in a real plasma, ν and κ are not independent of one another. EIC waves propagate according to the following (approximate) dispersion relation (for $T_e \gg T_i$, where T_e is the electron temperature and T_i is the ion temperature):[8]

$$\omega^2 = \omega_{ci}^2 + k^2 \frac{Z k_B T_e}{m} \tag{24}$$
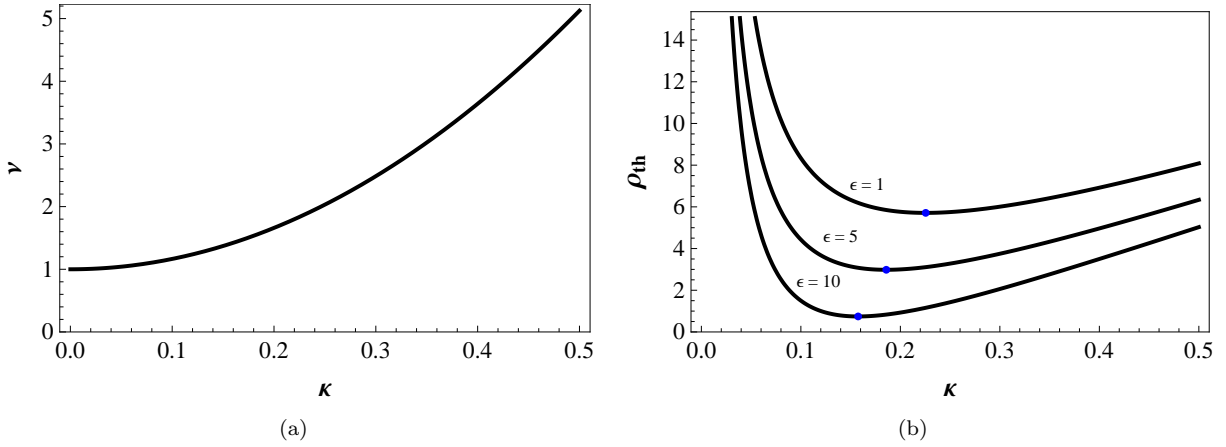
Figure 16. (a) Plot of the EIC dispersion relation for $T_r \approx 30$. (b) Plot of theoretical ρ_{th} values for various normalized wave amplitudes (again, for $T_r \approx 30$). Blue points represent minimum values of ρ_{th}.

where Z is the ion charge (in units of e). In $\bar{r}_L$-normalized coordinates, this expression becomes

$$\nu^2 = 1 + \kappa^2 \frac{ZT_r}{2} \tag{25}$$

where T_r is the ratio of the electron temperature to the ion temperature (T_e / T_i). By using this expression to relate ν and κ we introduce a degree of physical fidelity into our analysis that would be absent otherwise.

Next we consider self-consistency at its lowest order. We are investigating ion acceleration by beating electrostatic waves; however, in a real plasma, electrostatic waves propagate via perturbations in the electron and ion population. Thus, since all of our analysis up to this point has featured the use of constant wave parameters, we have implicitly assumed that the exciting waves are unaltered by ion dynamics. In reality, this limits the scope of our investigation to relatively small wave amplitudes $(\varepsilon \lesssim 10)$.[15]

Thus, by combining these limiting criteria with measured electron and ion temperature values, we can come up with a first-order approximation for the value of ρ_{th} in a real plasma. For the purposes of this investigation, we use BWXII temperature data collected by Jorns and Choueiri in 2010.[8] For a singly-ionized $(Z = 1)$ argon plasma, they measured electron and ion temperatures of 3 and 0.1 eV, respectively (thus, $T_r \approx 30$). Given that $T_e \gg T_i$, our expression for the dispersion relation (25) is valid. The resulting relationship between ν and κ is plotted in Figure 16(a). Note that EIC waves cannot propagate for $\nu < 1$ $(\omega < \omega_{ci})$.

Now that we have determined the relationship between ν and κ, we combine the dispersion relation with our small-amplitude approximation to determine allowable ρ_{th} values for various wave amplitudes. Figure 16(b) features ρ_{th} curves for $\varepsilon = 1$, 5, and 10. We clearly see that for a given wave amplitude, there is a corresponding minimum value of ρ_{th}. Given that we are seeking to minimize the stochastic threshold, we will refer to this minimum as the optimum value for ρ_{th}. We clearly see that for the given spectrum of allowable wave amplitude values, the universal optimum occurs for $\varepsilon = 10$. For this wave amplitude, the stochastic threshold is minimized when $\kappa \approx 0.16$ and $\nu \approx 1.47$, yielding an optimal ρ_{th} value of approximately 0.75. In subsequent analysis, we use these optimized wave parameters to deduce the specific impulse of the BWT via numerical simulation. Before proceeding, however, we recall that in the $\bar{r}_L$ normalization scheme, $\bar{\rho}$ is implicitly equal to one. Thus, for this particular set of physical wave parameters, $\rho_{th} < \bar{\rho}$. This implies that a significant portion of the ion population will undergo stochastic acceleration, which in turn will push trapped ions into the forward-drifting regime while simultaneously enhancing the X velocity of ions that are already-forward-drifting.

2. BWT Specific Impulse Estimate

After determining approximate wave parameters that optimize ρ_{th} for a physical plasma, we conducted numerical simulations to determine the average exhaust velocity of the BWT in the case of BEW propagation. We followed a procedure similar to that used in Section II to deduce the exhaust velocity of an unperturbed ensemble in a magnetic slope configuration. To start, we evenly distributed 10,000 ions in the X and Y

intervals $[0, 2\pi/\kappa]$ and $[-L, L]$, respectively. Note that the upper bound of the X interval is equal to the normalized wavelength, and was chosen due to the spatial periodicity of the exciting waves. The initial X and Y velocities of each ion were determined by sampling from the Maxwellian described in 8. The ensemble was assumed to be collisionless; only single-ion dynamics were considered in simulation. The exit plane wase located one wavelength $(2\pi/\kappa)$ from the upper bound of the X interval, and ions that breached this plane were considered part of the exhaust plume (which in the context of a two-dimensional geometry, is really an exhaust "sheet"). Their instantaneous velocity upon doing so was their exit velocity, denoted by V_X. For each individual ion, we monitored the numerical integration of Hamilton's equations at each time step to ensure that the ion remained within the Y limits set by the thruster bound L. Ions whose trajectories exceeded these bounds were considered lost to the walls. Numerical integration was performed over long timescales to minimize the error associated with low-velocity particles.

In conducting these simulations, it became immediately clear that the optimized geometry derived in Section II for the unperturbed case was not readily applicable to the perturbed case. However, this was to be expected for two reasons. In the unperturbed case, a geometry that features a large fraction of particles in the Larmor region is a mark of inefficiency; precessing particles can never break the exit plane of the thruster, and therefore cannot contribute to thrust generation. A principal benefit of BEW propagation, however, is its ability to push particles from Larmor precession into forward-drifting orbits. In the BEW case, the Larmor region can be thought of as a massive reservoir from which particles can be selectively drawn to alter the density of the current flowing along the magnetic null. Thus, a geometry that features a large number of initially-trapped particles is actually desirable (to a degree) in the BEW case. Another reason why the unperturbed optimized geometry is inapplicable in this case has to do with the fundamental nature of the BEW acceleration mechanism. The physical manifestation of BEW acceleration for an ion is a change in its Larmor radius. Upon breaking the stochastic threshold, an ion's Larmor radius dramatically increases and subsequently oscillates chaotically about some mean value greater than ρ_{th}. This notion, coupled with the fact that ions can only be pushed into forward-drifting orbits if they breach the stochastic threshold, implies that the population of forward-drifting ions that results from the introduction of BEW has a relatively large average ρ value. This also implies that while BEW can both increase and enhance flow in the X direction, it can also greatly increase the Y-range swept out by ions as they propagate forward in X. Thus, any BEW propagation in the context of the unperturbed optimized geometry (where $L = 1.6$) that would otherwise enhance current flow just results in an overwhelmingly large percentage of the ions being lost to the walls ($> 95\%$). Thus, a new thruster geometry had to be determined if the simulations were to have any meaning.

For the optimal wave parameters previously prescribed ($\varepsilon = 10$, $\kappa = 0.16$ and $\nu = 1.47$), numerical investigations of ion trajectories revealed that forward-drifting ions exhibited an upper bound in Y of approximately 50. Thus, we set $L = 50$ in the interests of increasing net ion flow while also decreasing the percentage of ions that collide with the thruster walls.

Figure 17 illustrates some of the major results of the simulation. Figure 17(a) depicts the velocity distribution of ions that breached the exit plane during the course of the BEW simulation. The distribution peaks around 25. The average value of this distribution – which is equal to the normalized exhaust velocity U_{ex} – is approximately 21. For an ion temperature of approximately 0.1 eV, this yields an I_{sp} value of approximately 1500 s for argon. For a hydrogen thruster with the same T_i, the corresponding I_{sp} value is nearly 9500 s. These values clearly represent a vast improvement over the unperturbed configuration, and puts the Beating Wave Thruster in the same I_{sp} range as many existing Hall and ion thruster configurations.[17]

Numerical results also indicated that the fraction of ions that break the exit plane (denoted by ξ_{ex}) is approximately 0.837. Note that ξ_{ex} in the perturbed case is approximately equivalent to ξ_f in the unperturbed case. Furthermore, the fraction of ions that escape to the walls of the thruster (ξ_{esc}) in the perturbed case is approximately 0.163. This implies that the percentage of ions that remain trapped in Larmor or reverse-drifting orbits during BEW propagation is $< 0.1\%$. This represents an astronomical increase in efficiency over the unperturbed case (where $\xi_f = \xi_{ex} \approx 0.535$, $\xi_{esc} \approx 0.349$, and the remaining 11.6% of ions were trapped in non-forward-drifting orbits). Thus, it is clear from these numerical results that BEW acceleration appreciably increases – and enhances – the net flow of ions in the X direction along the magnetic null.

For the purpose of comparison, Figure 17 also depicts the results of a simulation featuring SEW propagation for equal energy densities. An examination of the SEW exit velocity distribution featured in Figure 17(b) reveals a clear shift in both the peak and mean values of V_X. While the distribution peaks around 19, the average exhaust velocity U_{ex} is approximately 18. Furthermore, there are noticeably fewer high-velocity particles ($V_X \gtrsim 30$) in the SEW case as compared to the BEW case. Numerical results reveal that for SEW,

(a) Normalized exit velocity distribution (BEW).
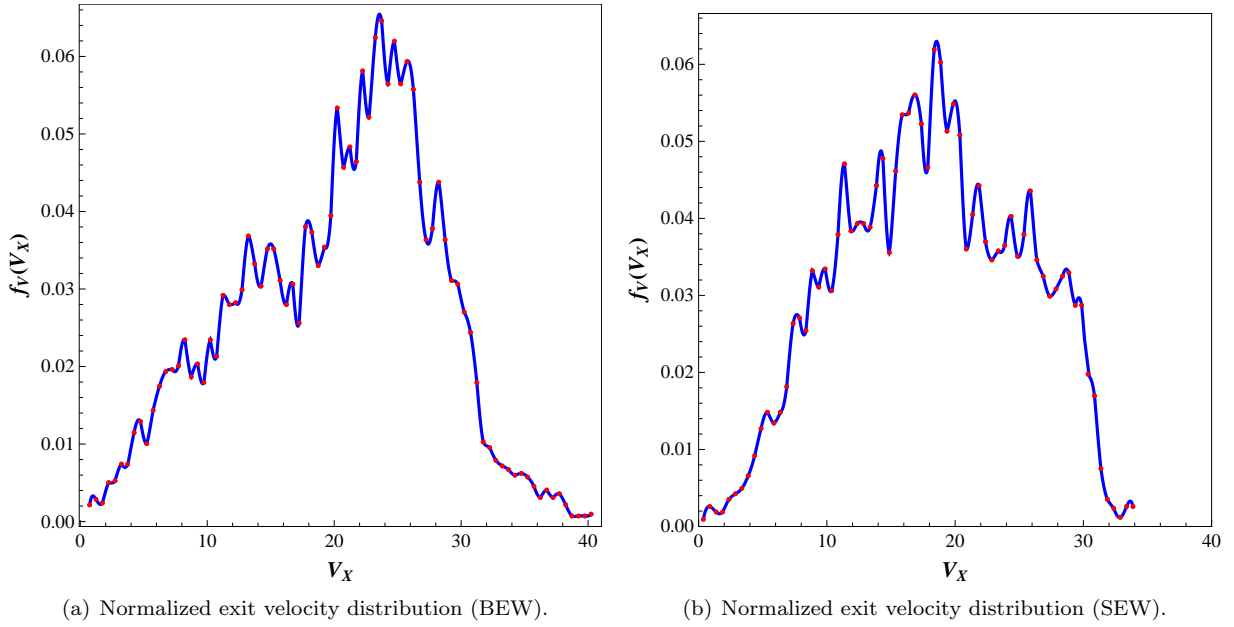

(b) Normalized exit velocity distribution (SEW).

Figure 17. Normalized exit velocity distribution plots for (a) BEW and (b) SEW. For SEW, $\varepsilon = 10\sqrt{2}$, $\kappa = 0.16$ and $\nu = 1.47$. For BEW, $\varepsilon = 10$, $\kappa = 0.16$ and $\nu_1 = 1.47$. In both cases, $\bar{\bar{\delta}} = 1/3$.

$\xi_{ex} \approx 0.850$ and $\xi_{esc} \approx 0.150$. These values are comparable to the corresponding BEW results. This makes sense given that the theoretical benefit of BEW over SEW in the context of wall loss minimization is due to the existence of a regular acceleration region. However, given the relative magnitudes of $\bar{\rho}$ and ρ_{th}, the regular acceleration region is negligibly small in this case; thus, for the chosen wave parameters, BEW and SEW propagation result in comparable levels of ion channeling.

From U_{ex}, we can calculate theoretical specific impulse values for the single wave case. Using the same plasma parameters that we used to calculate BEW I_{sp}, the corresponding SEW I_{sp} values for argon and hydrogen fuel are 1275 s and 8000 s. These values represent a 15% decrease in I_{sp} relative to BEW levels for equal energy densities.

Thus, in the context of the chosen wave parameters, while BEW and SEW result in similar wall losses, beating wave propagation results in a higher exhaust velocity (and thus, I_{sp}). Since the stochastic threshold ρ_{th} is so low relative to $\bar{\rho}$ (such that the regular acceleration is negligibly small), these results suggest that BEW acceleration may feature a more effective stochastic acceleration process than SEW. This is yet another topic of potential further theoretical investigation.

3. BWT Thrust Estimate

Recall the linear thrust density equation derived in Section II:

$$\frac{T}{\ell} = 2^{5/2} \left(\xi_{ex} L_{max} U_{ex}^2 \right) \frac{n\sqrt{m}(k_B T_i)^{3/2}}{q B_0} \tag{14}$$

where we have replaced ξ_f with ξ_{ex}. Citing the figures reported in the previous section ($L_{max} = 50$, $U_{ex} = 21$, and $\xi_{ex} = 0.837$), we can use this expression to calculate theoretical thrust values for the Beating Wave Thruster. If we again assume that $n \approx 10^{10}$ cm^{-3}, $T_i \approx 0.1$ eV, and $B_0 \approx 500$ Gauss, the approximate thrust densities for argon and hydrogen are 0.07 N/m and 0.01 N/m, respectively (the corresponding SEW thrust densities are nearly 30% smaller). Not only does this represent a significant improvement over unperturbed thrust levels, but it also indicates that from the perspective of thrust generation, the Beating Wave Thruster can compete with many existing (and currently operational) ion and Hall thruster configurations.[17] Thus, while these thrust values are approximate, they are encouraging nonetheless.

From Eq. 14, we can see how thrust density scales with various plasma parameters. For a given pair of beating waves and a fixed (normalized) thruster geometry (i.e. fixed ξ_{ex}, L_{max}, and U_{ex}), we see that there

are several ways to increase the thrust density of the BWT. In choosing a propellant to maximize thrust, high ion mass and low ion charge are desirable. However, we see from the definition of u_{ex}:

$$u_{ex} = U_{ex}\sqrt{\frac{2k_B T_i}{m}} \tag{26}$$

that greater ion mass also results in reduced exhaust velocity (and thus, reduced I_{sp}). Thus, in terms of fuel selection, there is a clear tradeoff between thrust density and specific impulse.

Thrust density also increases with ion density n. However, as will be briefly discussed in Section V the next section, there is an upper limit to the allowable ion density for a given ion temperature due to the potentially negative effects of collisional processes on thruster performance.

4. Optimization Procedure

The L value that was used in this particular simulation was determined based on a combination of intuition and small-scale investigation of ion trajectories. In this section, however, we consider a potential procedure for optimizing the BWT geometry so as to maximize thruster performance.

First, it is clear that to minimize wall losses, it is desirable for $L > |Y_{UB}|$, where $|Y_{UB}|$ is the approximate upper Y bound of forward-drifting ion trajectories for a given set of wave parameters. Furthermore, given that BEW acceleration (like its SEW counterpart) has an upper bound in ρ (ρ_{UB}), it is obvious that L cannot be made arbitrarily large, otherwise particles near the walls would never be able to reach the magnetic null (for a collisionless plasma). However, given that BEW stochastic acceleration also causes a net shift in the guiding center towards the magnetic null, this implies that a particle with $|Y_{GC}| > \rho_{UB}$ can still potentially reach the null and be pushed into the forward-drifting region. We will refer to the maximum $|Y_{GC}|$ value for which this phenomenon occurs as $|Y_{GC,max}|$. From these observations, we conclude that while $L > |Y_{UB}|$ will help to significantly minimize walls losses, the optimal L value (in terms of the total number of ions that can be pushed into forward-drifting orbits via BEW propagation) for the perturbed case lies somewhere in the vicinity of $|Y_{GC,max}|$ (which numerical results reveal tends to be much larger than $|Y_{UB}|$). However, in order to determine the actual optimum geometry for a given pair of beating waves, we need explicit expressions for both $|Y_{UB}|$ and $|Y_{GC,max}|$, neither of which have been (accurately) theoretically defined. Thus, further developments in this area would allow us to effectively optimize BWT geometry from the standpoint of both mass flow (thrust generation) and wall loss minimization.

IV. Preliminary Proof-of-Concept Design

Preliminary simulation has clearly shown that the BWT has potential as an electric propulsion concept. Thus, while developing BEW theory and simulation architecture is very important, so is the demonstration of BWT performance in a laboratory setting. Thus, a proof-of-concept experiment is a critical next step in the actual development of BWT technology. It is our intention to adapt BWXII for this very purpose.

One of the most important aspects of the proof-of-concept experiment is going to be the accurate reproduction of a steeply-sloped magnetic field within the vacuum chamber. In their original paper, Jorns and Choueiri proposed a thruster design that featured the use of two parallel current sheets to produce the desired magnetic field (see Figure 18(a)).[1] However, this design is insufficient. While finite current sheets would indeed produce a magnetic slope, the slope would be extremely shallow and occupy the vast majority of the span between the two plates. This becomes apparent when one takes the limit of very large plates, since the magnetic field between two infinite current sheets with parallel currents is identically zero. Thus, since the BWT concept calls for a steep magnetic slope, the current sheet geometry is not applicable when trying to reproduce the idealized field configuration used in our previous analysis.

One simple configuration that can effectively reproduce the necessary field configuration to a very good approximation is featured in Figure 18. An antisymmetric arrangement of current loops (or Helmholtz coils) is shown at the $x = 0$ cross-section of the y-z plane. Axial vectors of each current loop point in the z-direction. Loops in quadrants I and IV have current flowing in one direction; loops in quadrants II and III have current flowing in the opposite direction. This produces a magnetic field with two near-homogeneous regions of opposite polarity, and a magnetic null (coupled with a sharp magnetic slope) at their interface. Linear ion current flows out of the page in the positive x-direction.
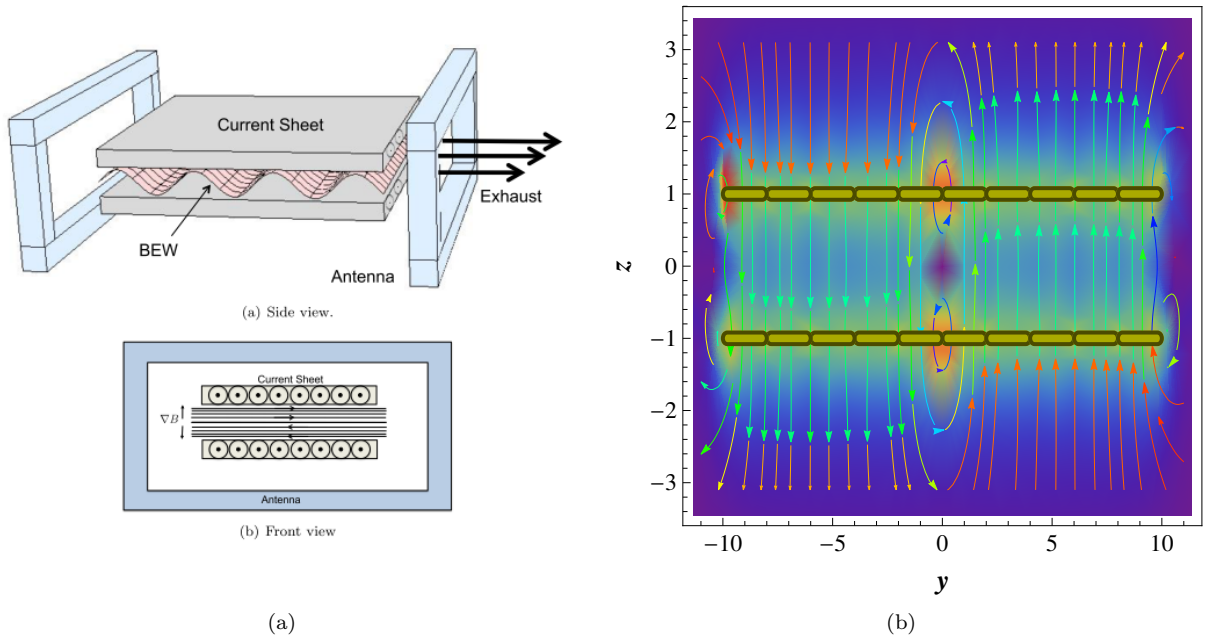
Figure 18. (a) Originally proposed configuration featuring the use of two current sheets to produce a sloped magnetic field (taken from Ref.[1]). However, this design does not result in a steep magnetic slope. (b) Magnetic field vector and density plot for an antisymmetric configuration of current loops. By inspection, we see that for a given z-value between -1 and 1, the field is approximately homogeneous for $1 < |y| < 9$, features a magnetic null at $y = 0$, and is steeply-sloped in the interval $|y| < 1$. The positive x-axis (and thus, the direction of the net ion current) points out of the page.

A sampling of field magnitudes along $z = 0$ was taken to deduce field dependence on y. Parameters were scaled appropriately in an attempt to match the theoretical field described by (1). Figure 19 features a plot of the numerical data deduced from the above sampling, as well as the hyperbolic tangent field profile described by (1) for $B_0 = \delta = 1$. Aside from minor field oscillations and fringe effects at large y, the current loop field matches the theoretical field very well, suggesting that this simple current loop configuration could be an effective way of producing the desired field in a laboratory setting. Furthermore, while permanent magnets could be used to produce a similar magnetic field topography, the use of current loops allows for B-field tuning (and thus the adjustment of grad-B in the sloped region) since $B \propto I$. Once BWT thrust and I_{sp} levels have been successfully measured in the laboratory, they can be used to cross-check the theory developed both in this thesis and in the seminal paper of Jorns and Choueiri,[1] and ultimately, to spur the development of an actual thruster design.

V. Discussion

We have effectively demonstrated via numerical simulation and subsequent calculations that BEW propagation increases both the velocity and density of the linear ion current that forms along the null of a steeply-sloped rectilinear magnetic field for a thermalized ion ensemble. We have also demonstrated that the "ion channeling" characteristic of BEW acceleration helps to mitigate wall losses that plague other electric thrusters. Theoretical specific impulse and thrust density values indicate that BEW direct ion acceleration can be an effective propulsion mechanism, and therefore, that the BWT has potential as a future electric propulsion device.

However, in spite of these promising results, our analysis featured a number of simplifying assumptions. Several factors were neglected that could impact BWT performance. We discuss the relative impacts of those factors here.
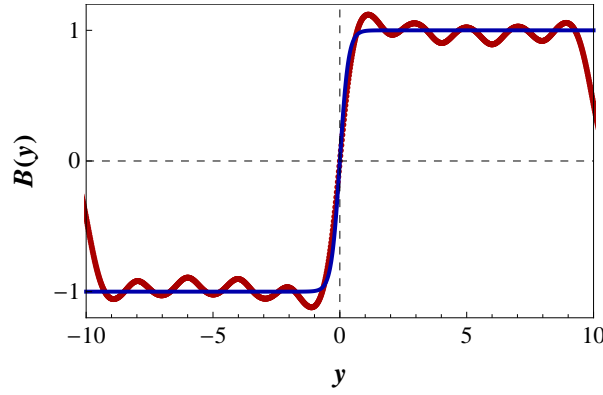
Figure 19. Magnetic field for the above current loop configuration along z = 0 (red curve). The blue curve is a theoretical field (1) **with** $B_0 = \delta = 1$.

1. Collisions

In the context of BEW acceleration, an important quantity to consider when evaluating the effects of collisions on ensemble behavior is the Hall parameter, which is defined as the ratio of the gyrofrequency to the collision frequency:[17]

$$\Omega_i = \frac{\omega_{ci}}{\nu_c} \tag{27}$$

Since the BWT concept exploits the Larmor motion of particles to produce a linear ion current, we conclude that if $\Omega_i < 1$, in all likelihood, the effectiveness of the BWT will decrease dramatically. For ion-ion collisions, the collision frequency ν_i goes as $n_i T_i^{-3/2}$ (where n_i is the ion density).[18] Thus, for a given plasma (i.e. fixed ion charge and mass), we can increase the Hall parameter by increasing the magnitude of the magnetic field, decreasing the ion density, and/or increasing the ion temperature.

2. Multiple Species

In the above analysis, the coupling of energy from the wave to the electrons can largely be ignored since the wave frequency is too long to induce stochastic effects in electron orbits. However, since the ions will be subject to significant drifts due to the BEW, ambipolar effects will undoubtedly play a role in thruster performance.

Jorns and Choueiri theorized that the ejection of ions from the end of the thruster geometry would create an ambipolar electric field of sufficient strength to drag the electron population with it, thereby ensuring the quasi-neutrality of the exhaust.[1] However, the induced electric field may adversely effect the performance of the BEW acceleration mechanism. This in turn could have a negative impact on both BWT thrust and specific impulse values.

It is difficult to examine these effects with our simplified numerical scheme; however, Particle-in-Cell (PIC) codes (which are generally much more complex than the Monte Carlo methods featured in this paper) may be employed to accurately capture two-species ensemble behavior.[19]

3. Self-Consistency

As aforementioned, we have assumed that the exciting waves are unaltered by ion dynamics. In reality, however, BEW propagate via perturbations in the electron and ion populations within a plasma. In our analysis, we limited the amplitude of the exciting waves ($\varepsilon < 10$) to minimize the error associated with the absence of self-consistency. However, these self-consistent effects can be introduced and characterized via the aforementioned PIC codes. These complex models would allow us to increase ε while mitigating error, and since increasing the wave amplitude decreases the time scale on which BEW acceleration occurs, it is likely that these self-consistent simulations will result in even higher BWT thrust density and specific impulse figures. To conduct such a numerical investigation on a large scale, however, would likely require a very complex base code, coupled with significant computational power.

VI.   Conclusions

The goal of this investigation was to demonstrate the feasibility and validity of a new plasma propulsion concept that uses beating electrostatic waves to augment the linear ion current generated by a thermalized ion ensemble in a rectilinear magnetic slope geometry.

After describing thruster fundamentals – magnetic topography, single-ion dynamics, orbit domains – we extended our analysis to a thermalized ion ensemble via numerical simulation. An optimal unperturbed thruster configuration was numerically deduced, and simulation results unambiguously demonstrated that a rectilinear, steeply-sloped magnetic field does indeed produce a net linear ion current that flows along the magnetic null. Benchmark specific impulse and thrust density values were determined, and unperturbed thruster performance was shown to be very poor.

After the introduction of the perturbed case, an investigation of ion dynamics for $\varepsilon \neq 0$ was conducted that expanded on the previous work of Jorns and Choueiri.[1] It was shown that stochastic acceleration was required in order for trapped ions to be pushed into forward-drifting orbits, and that already-forward-drifting ions were often decelerated if $\rho_0 < \rho_{th}$. The "ion channeling" phenomenon was demonstrated numerically, in which stochastic ions are preferentially transported away from the thruster walls and towards the magnetic null. It was ultimately deduced that to a large degree, the magnitude of ρ_{th} essentially dictates thruster performance. The EIC dispersion relation was then introduced and wave amplitudes were limited to preclude self-consistent effects. Numerical simulations featuring both single and beating electrostatic wave propagation using optimal wave parameters were conducted to deduce resulting thruster characteristics. It was ultimately demonstrated that (for the given wave parameters) while SEW and BEW performed similarly in terms of wall loss minimization, BEW was superior in both thrust generation and specific impulse. The BWT was thus shown to possess specific impulse and thrust levels comparable to existing ion and Hall thruster configurations (for argon, $I_{sp} \approx 1500$ s and $T/\ell \approx 0.07$ N/m). Nearly 85% of ions were shown to contribute to the BWT exhaust plume, while only 15% of the initial ion population was shown to escape to the thruster walls.

Based on these preliminary results, it is reasonable to assert that the BWT concept has the potential to form the basis of a new class of electrodeless, efficient, and variable electric thruster that rivals – and could potentially surpass – the performance of operational ion and Hall thrusters. As such, the further investigation and optimization of this novel ion acceleration mechanism is strongly encouraged.

References

[1]Jorns, B. and Choueiri, E. Y., "A Plasma Propulsion Concept Based on Direct Ion Acceleration with Beating Electrostatic Waves," *American Institute of Aeronautics and Astronautics*, 2010, pp. 1–19.

[2]Mozer, F. S., Carlson, C. W., Hudson, M. K., Torbert, R. B., Parady, B., Yatteau, J., and Kelley, M. C., "Observations of Paired Electrostatic Shocks in the Polar Magnetosphere," *Physical Review Letters*, Vol. 38, No. 6, 1977, pp. 292–6.

[3]Sankaran, K., Cassady, L., Kodys, A. D., and Choueiri, E. Y., "A survey of propulsion options for cargo and piloted missions to Mars." *Annals of the New York Academy of Sciences*, Vol. 1017, May 2004, pp. 450–67.

[4]Wilbur, P., Jahn, R., and Curran, F., "Space electric propulsion plasmas," *IEEE Transactions on Plasma Science*, Vol. 19, No. 6, 1991, pp. 1167–1179.

[5]Ahedo, E., Gallardo, J. M., and Martinez-Sanchez, M., "Effects of the radial plasma-wall interaction on the Hall thruster discharge," *Physics of Plasmas*, Vol. 10, No. 8, July 2003, pp. 3397.

[6]Spektor, R., *Ion Energization by a Pair of Beating Electrostatic Waves*, Ph.d., Princeton University, 2006.

[7]Chest, E., Estublier, D., Fallis, B., Gengembre, E., Gonzalezdelamo, J., Kutufa, N., Nicolini, D., Saccoccia, G., Casalino, L., and Dumazert, P., "Flexible variable-specific-impulse electric propulsion systems for planetary missions," *Acta Astronautica*, Vol. 59, No. 8-11, Oct. 2006, pp. 931–945.

[8]Jorns, B. and Choueiri, E. Y., "Optimal Frequency for Plasma Heating with a Single Electrostatic Wave," *Joint Propulsion Conference*, , No. July, 2010.

[9]Ram, A. K., Bers, A., and Benisti, D., "Ionospheric ion acceleration by multiple electrostatic waves," *Journal of Geophysical Research*, Vol. 103, No. A5, 1998, pp. 9431–9440.

[10]Benisti, D., Ram, A. K., and Bers, A., "Ion dynamics in multiple electrostatic waves in a magnetized plasma. I. Coherent acceleration," *Physics of Plasmas*, Vol. 5, No. 9, 1998, pp. 3224.

[11]Benisti, D., Ram, A. K., and Bers, A., "Ion dynamics in multiple electrostatic waves in a magnetized plasma. II. Enhancement of the acceleration," *Physics of Plasmas*, Vol. 5, No. 9, 1998, pp. 3233.

[12]Spektor, R. and Choueiri, E. Y., "Ion acceleration by beating electrostatic waves: domain of allowed acceleration." *Physical Review E - Statistical, Nonlinear and Soft Matter Physics*, Vol. 69, No. 4 Pt 2, 2004, pp. 046402.

[13]Spektor, R. and Choueiri, E. Y., "Measurements of Ion Energization by a Pair of Beating Electrostatic Ion Cyclotron Waves," *International Electric Propulsion Conference*, 2005, pp. 1–11.

[14] Jorns, B. and Choueiri, E. Y., "Experiment for Plasma Energization with Beating Electrostatic Waves," *International Electric Propulsion Conference*, 2009, pp. 1–11.

[15] Jorns, B. and Choueiri, E. Y., "Ion Heating with Beating Electrostatic Waves," *Physical Review Letters*, Vol. 106, No. 8, Feb. 2011.

[16] Karney, C. and Bers, A., "Stochastic Ion Heating by a Perpendicularly Propagating Electrostatic Wave," *Physical Review Letters*, Vol. 39, No. 9, Aug. 1977, pp. 550–554.

[17] Jahn, R. G., *Physics of Electric Propulsion*, Dover Publications Inc., Mineola, N.Y., 1996.

[18] Goldston, R. J. and Rutherford, P. H., *Introduction to Plasma Physics*, Institute of Physics Pub., 1995.

[19] Birdsall, C. K. and Langdon, A. B., *Plasma physics via computer simulation*, Taylor & Francis, 2004.